Self-Sealing of Fractures in indurated Claystones

GRS - 704

Gesellschaft für Anlagen-
und Reaktorsicherheit
(GRS) gGmbH

Self-Sealing of Fractures in indurated Claystones

Experimental Study as Part
of the EC Joint Project
EURAD WP 6 - GAS

Final Report

Chun-Liang Zhang
Abram Rogalski
Oliver Czaikowski

January 2024

Remark:

This report was prepared under grant agreement No. 847593 with the European Union's Horizon 2020 research and innovation programme (EURAD) and under contract No. 02E11627 with the German Federal Ministry for the Environment, Nature Conservation, Nuclear Safety and Consumer Protection (BMUV).

The work was conducted by Gesellschaft für Anlagen- und Reaktorsicherheit (GRS) gGmbH.

The authors are responsible for the content of this report.

GRS - 704
ISBN 978-3-949088-95-7

Keyword

Experimental study, fracture closure, gas migration, hydromechanical behaviour, indurated clay rock, self-sealing, water permeability

Foreword

In the framework of the European Joint Programme on Radioactive Waste Management (*EURAD*) – Work Package 6 – GAS, GRS investigated gas transport and impact on self-sealing of fractures in the indurated Callovo-Oxfordian (COX) and Opalinus (OPA) claystones. Core samples were extracted from four lithological facies relatively rich in clay mineral, carbonate and quartz, respectively. They were artificially cracked to different fracture intensities. Self-sealing of the fractures was measured by fracture closure, water permeability variation, gas penetration, and recovery of gas-induced pathways. Most of the fractured samples exhibited a dramatic reduction in water permeability to very low levels close to that of the intact clay rocks, depending on their mineralogical composition, fracture intensity, confining stress, and load duration. The self-sealing capacity of the clay-rich samples is higher than that of the carbonate-rich and sandy ones. Significant effects of sample size and fracture intensity were identified. The sealed fractures become gas-tight for certain injection pressures. However, the measured gas breakthrough pressures are still lower than the confining stresses. The gas-induced pathways can reseal when contacting water. These important findings imply that fractures that will be generated by excavation of a repository in such a clay host rock can seal with time.

Table of contents

1 Introduction

Clay formations are world-widely investigated for deep geological disposal of radioactive waste due to their favourable properties such as large homogeneous rock mass, stable geological structure, extremely low hydraulic conductivity, certain self-sealing potential, diffusion-dominated transport, and high sorption capacity for radionuclides. In France and Switzerland, for instance, the potential repositories were proposed to be constructed in the hardened Callovo-Oxfordian (COX) and Opalinus (OPA) clay formations respectively /AND 05/ /NAG 02/. In Germany, exemplarily for different geological conditions, two generic models were developed based on the known data for the Lower Cretaceous Clay (northern Germany) and the Opalinus Clay (southern Germany) /JOB 17/. The main purpose was to elaborate the methodology of demonstration of the safety of a repository for high-level radioactive waste (HLW) in clay formations according to the German regulations.

Excavation of an underground repository will unavoidably generate a damaged zone (EDZ) around the openings and can rise the permeability up to several orders of magnitude, as observed in the Underground Research Laboratories (URLs) at Bure /ARM 14/ /DE 15/ and at Mont-Terri /BOC 17/ /HAL 21/. Thanks to the self-sealing capacity of the claystones, a gradual hydraulic recovery of the EDZ can be expected during the post-closure phase limiting water flow and radionuclides transport to the biosphere. Another concern is gas generation and migration. Over thousands of years, gases will be produced mainly from anoxic corrosion of metallic materials remained /ROD 99/. With accumulation of gases in the closed repository, gas pressure could rise and may exceed certain thresholds to damage the integrity of the host rock and engineered barriers. Two important questions on the gas issue are to be answered: a) whether the EDZ after sealing can still allow gas release without over-pressurisation to damaging the geological-engineered barrier system; and b) whether the gas-induced pathways can reseal again to hinder transport of water and radionuclides.

In the last two decades, water and gas transport behaviour in fractured COX and OPA claystones have been extensively investigated on samples in laboratory experiments /BOC 10/ /ZHA 11/13/15/ /AUV 15/ /GIO 18/ /DON 19/ and in field experiments at URLs Bure /DE 15/ and Mont-Terri /MAR 17/. Most of the studies focused on self-sealing of fractures in the clay-rich facies of COX and OPA formations. Significant self-sealing capacities of the clay-rich claystones were evidenced by fracture closure and permeability reduction under combined impact of mechanical compression and water-induced clay

swelling. Micro- and macrocracks in the clay-rich claystones can strongly self-seal to very low water permeability values of 10^{-18} – 10^{-21} m^2 close to the intact rock, even at low confining stresses of 2 – 4 MPa within months to years. For gas entry and penetration through water-saturated and sealed fractures, even if pressures required to overcome the capillary thresholds of the sealed pathways are high, they are still lower than the confining stresses and lower than the threshold pressure in the intact rock. This implies that gases generated in a repository can release preferably through the EDZ without compromising the integrity and barrier functions of the host rock and engineered barriers.

As well known, the sedimentary clay formations consist of layered lithological facies with different mineralogical compositions, petrophysical and hydro-mechanical properties /HOR 96/ /MAZ 08/ /BOC 10/. The OPA formation can be divided into three layered lithological facies: 1) clay rich shaly facies – a dark grey silty calcareous shale and argillaceous marl in the lower half of the sequence; 2) sandy-carbonate rich facies – a grey sandy and argillaceous limestone in the middle of the sequence; and 3) sandy facies – silty to sandy marls with sandstone lenses cemented with carbonate in the upper part /THU 99/ /PEA 03/ /BOS 17/. Figure 1.1 shows the geological structure of the OPA formation at URL Mont-Terri. The COX formation consists of three major geological units: clay rich unit (UA) at the base, transition unit (UT) and silty-carbonated unit (USC) /ROB 15/ /CON 18/. Figure 1.2 shows the variations of the major mineralogical compositions across the thickness of the COX formation. For the safe isolation of radioactive waste in the clay host rocks, all the lithological facies are to be precisely characterized and well understood.

Following the previous studies on the self-sealing behaviour of the clay-rich claystones /ZHA 11/13/15/, more recent investigations focused on self-sealing performance of fractures in the COX carbonate-rich and OPA sandy claystones in the framework of the European Joint Programme on Radioactive Waste Management (*EURAD*). The work was involved in the Work Package WP 6 - GAS focusing on the mechanistic understanding of gas transport in natural and engineered clay barriers. One task (Task 3) investigates hydro-mechanical phenomena and processes associated with gas-induced failure of the clay barriers (Subtask 3.1) and with self-sealing of gas-induced pathways in the clay barriers (Subtask 3.2). For Subtask 3.1, GRS measured water permeability, gas penetration and resealing of gas-induced pathways in the intact COX claystone. For Subtasks 3.2, long-term consolidation tests with water and then gas injection were undertaken on artificially fractured samples of different sizes and fracture intensities. Large samples of multi-decimetric length were used to cover the mineralogical variability of the clay rock,

particularly the COX carbonate-rich unit. Two specific apparatuses were developed for parallel testing on several samples under identical hydro-mechanical conditions. The self-sealing performance of fractures was characterized by fracture closure, water permeability change, gas breakthrough pressure, and recovery of gas-induced pathways, respectively. The research work and results achieved are presented in this report. Chapter 2 describes the basic characteristics of the sample materials and experimental methods applied. Experimental results obtained from the intact and fractured claystones are presented and analysed in chapter 3. Main conclusions will be drawn in chapter 4.

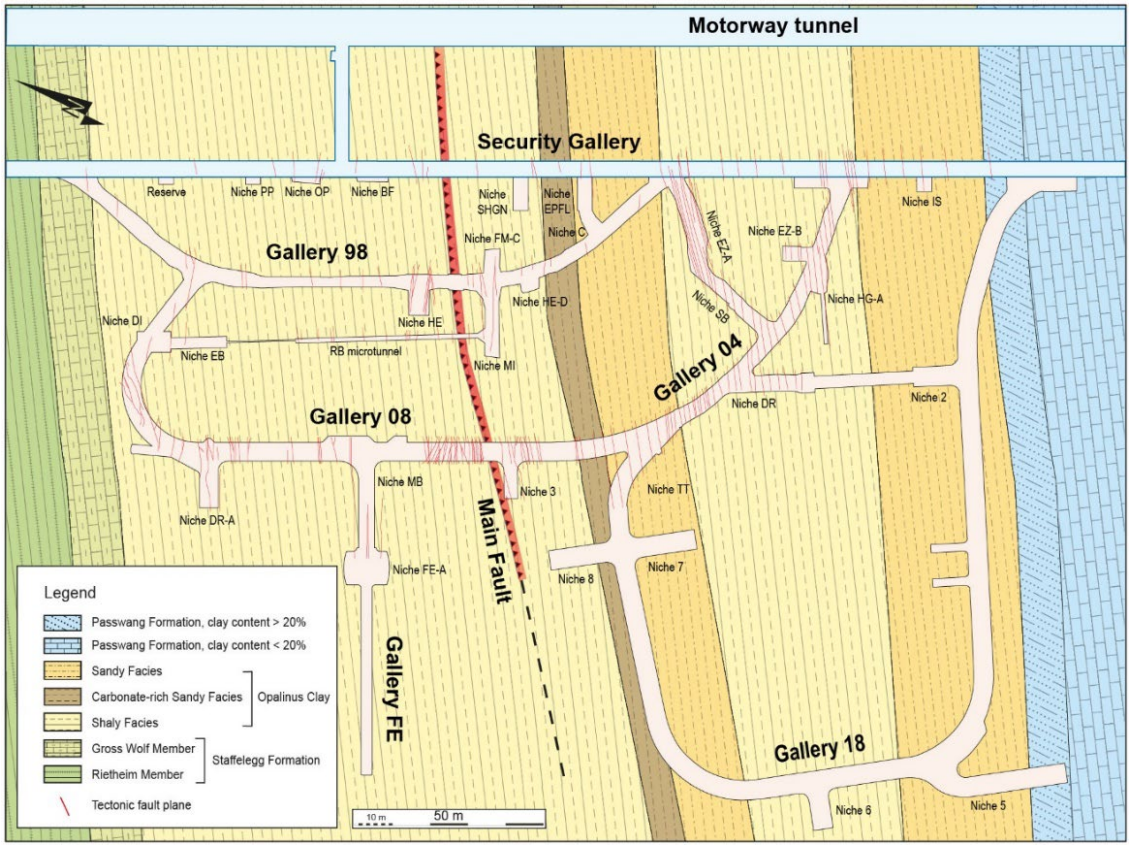

Fig. 1.1 Geological structure map and horizontal cross section of the Underground Rock Laboratory Mont-Terri (Swisstopo, 2019)

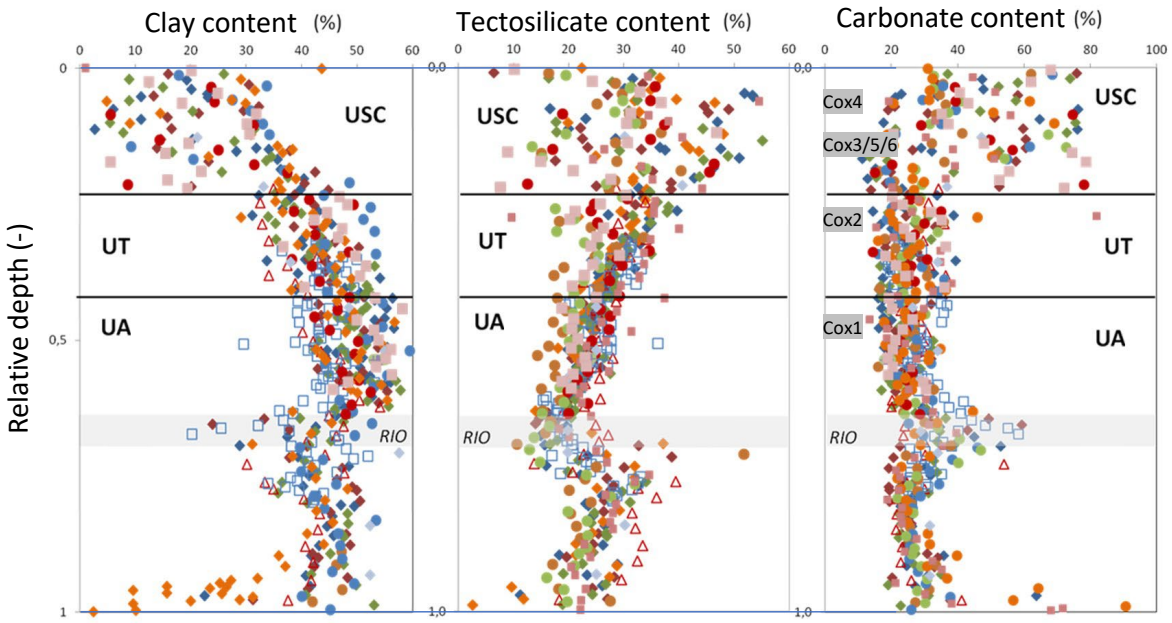

Fig. 1.2 Variation in mineralogical composition across the thickness of the COX formation (Andra, 2018). Data come from different boreholes and the relative depth is between the top of the USC unit and the bottom of the UA unit – locations of the studied samples

2 Characterization of samples

2.1 Mineralogical composition

Core samples were extracted from the sandy facies of OPA at URL Mont-Terri, from the three units of clay-rich (UA), transition (UT) and carbonate-rich (USC) of COX at URL Bure, respectively. They have different mineralogical compositions, petrophysical and hydro-mechanical properties. Table 1 summarises the variation ranges of their main mineralogical components: clay minerals, quartz, and carbonates. Compared to the COX clay-rich unit and OPA shaly facies, the COX carbonate-rich unit and OPA sandy facies have less clay minerals but more carbonates and quartz. The mineralogical composition of each facies displays a spatial variability. The OPA sandy facies is more heterogeneous on mm – cm scale than the shaly facies /KAU 13/ /HOU 14/. For instance, the samples taken from the OPA sandy facies for the present tests showed a large mineralogical variability within a short interval of 5 m with clay contents of 24 – 39 %, quartz of 34 – 39 %, carbonates of 15 – 33 %, and feldspar of 8 – 9 % (table 2). Similarly, a mineralogical heterogeneity appears in the COX carbonate-rich unit on cm – dm scales as observed at a drift front at the -445 m level of the URL Bure (figure 2.1). A sample from this area showed a large carbonates content of 50 %, quartz of 25 %, and a small clay content of 21 % (table 2). The mineralogical heterogeneity can lead to local differences in deformability, swelling capacity and thus self-sealing capacity of the rock mass. Generally, the swelling capacity of a claystone is determined by the fraction of clay minerals. The previous swelling experiments /ZHA 10/17/19/ showed that the studied claystones have swelling capacities to a large volumetric increase up to 10 % at the COX clay rich and OPA shaly facies and to 5 % at the OPA sandy facies. The swelling upon water uptake leads to degradation of the inner structure and reduction of the stiffness and strength.

Tab. 2.1 Main mineralogical components of the sandy and shaly facies of OPA formation and the carbonate-rich, transition and clay-rich unit of COX formation

Main component (%)	OPA[1] sandy facies	OPA[1] shaly facies	COX[2] carbonate-rich (USC)	COX[2] transition unit (UT)	COX[2] clay-rich unit (UA)
Clay minerals	20 – 40	55 – 75	15 – 40	30 – 55	40 – 55
Carbonates	15 – 40	5 – 30	20 – 80	20 – 40	20 – 35
Quartz	30 – 45	5 – 25	20 – 40	20 - 40	17 - 27

1: estimated based on /THU 99/ /MAZ 08/ /BOC 10/ /KAU 13/

2: estimated based on /AND 06/ /ROB 15/ /CON 18/ /GIO 18/

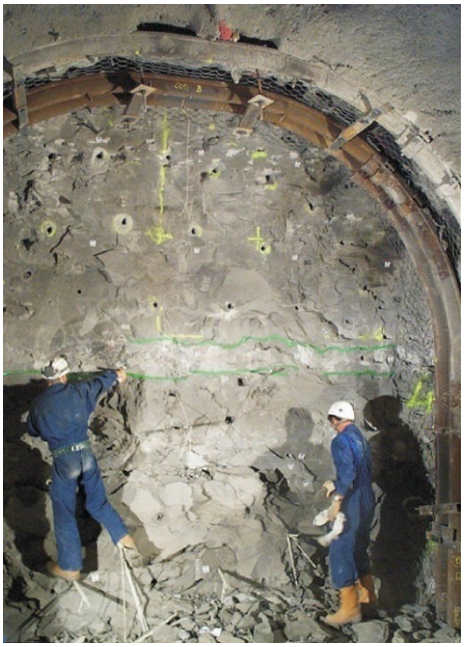

Fig. 2.1 Heterogeneous distribution of carbonates (light grey) in the COX carbonate-rich unit observed in a drift at the -445 m level of the URL Bure (Andra)

Tab. 2.2 Main mineralogical components of some tested samples

Core samples	Borehole depth (m)	Clay (%)	Quartz (%)	Carbonates (%)	Feldspar (%)	Others (%)
OPA sandy facies						
BDM-B9-9	8.2	24	34	33	9	< 1
DBM-B9-18	10.2	36	39	15	9	< 1
DBM-B9-29	12.8	39	38	15	8	< 1
COX carbonate-rich unit						
EST52337	2.9	21	25	50	4	< 1

2.2 Sample preparation

2.2.1 Intact samples

For testing intact claystone, two COX cores EST58148 and EST60765 of 80 mm diameter and 300 mm length each were extracted from a horizontal borehole OHZ3007 parallel to the bedding plane at the main level (-490m) of the URL Bure. After drilling, the cores were immediately sealed and confined in specific cells and stored in a storage hall at the surface. A year later, they were delivered to GRS for testing. Two samples were prepared to a diameter of D = 70 mm and lengths of L = 40 mm and 50 mm, respectively. Figure 2.2 shows some pictures of the sample preparation. After unpacking the cores from the cells, the top part of about 80 mm length with some damage was sawed off for measuring water content. From the intact part, samples were sawed off and prepared by shaving the peripheral and end surfaces in a lathe to a cylinder of D=70 mm and L = 40 mm for EST58148 and L = 50 mm for EST60765. In order to minimize desaturation, the sample was wrapped in thin plastic foil during the preparation. Figure 2.3 pictures the prepared sample EST60765. It shows very compact without visible fissures. Another prepared sample EST58148 was also quite intact without visible fissures.

The prepared sample was characterized by measuring the basic petrophysical proerties according to the testing methods suggested by International Society for Rock Mechanics /ISR 81/. The properties include grain density, dry density, bulk density, porosity, water content, and degree of water saturation, which are defined as follows:

Grain density: $\rho_s = \frac{M_s}{V_s}$ (2.1)

M_s = mass of solids, V_s = volume of solids.

Bulk density: $\rho_b = \frac{M}{V} = \frac{M_s + M_w}{V}$ (2.2)

M = mass of bulk sample, V = volume of bulk sample, M_s = mass of solids, M_w = mass of water.

Dry density: $\rho_d = \frac{M_s}{V}$ (2.3)

Porosity: $\varphi = \frac{V_v}{V} = \left(1 - \frac{\rho_d}{\rho_s}\right)$ (2.4)

V_v = volume of voids.

Water content: $$w = \frac{M_w}{M_s} \quad (2.5)$$

Degree of water saturation:

$$S_w = \frac{V_w}{V_v} = \frac{\rho_d \cdot w}{\rho_w \cdot \varphi} \quad (2.6)$$

The water content was measured on the top parts with a weight of ~750 g. They were dried in an oven at temperature of 105 °C for two days. The bulk density of the intact samples was determined by measuring the volume and weight. On basis of the measured bulk density and the water content, the dry density was calculated. The grain density was measured on the powder produced during sample preparation by means of pycnometer with helium gas. The porosity was obtained on basis of the measured grain and dry densities according to equation (4). The degree of water saturation was determined from the calculation according to equation (6). The basic characteristics of the intact samples are summarized in table 2.3. Because the samples were perfectly preserved against water loss, high degrees of water saturation remained at 93 – 100 %.

Delivered core EST60765

Partly damaged after unpacking

Cutting the damaged piece for measuring water content

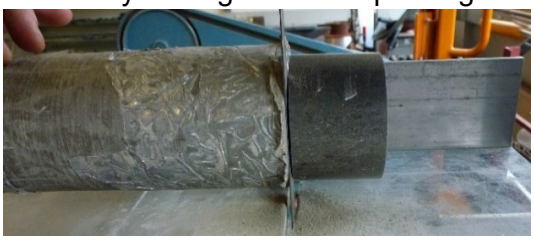

Cutting the intact piece for testing

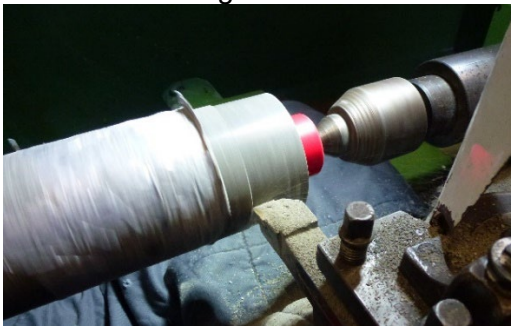

Shaving the peripheral surface

Planishing the end face

Fig. 2.2 Pictures of of the sample preparation



Peripheral surfaces 0-180°



Peripheral surfaces 180-360°


Top end face


Bottom end face

Fig. 2.3 Some pictures of the prepared sample EST60765

Tab. 2.3 Basic characteristics of the intact samples

Sample	Size D/L (mm)	Mass (g)	Grain density (g/cm^3)	Bulk density (g/cm^3)	Dry density (g/cm^3)	Porosity (%)	Water content (%)	Saturation degree (%)
EST58148	70/40	375.85	2.695	2.442	2.273	15.67	6.92	100.0
EST60765	70/50	458.75	2.700	2.401	2.230	17.30	7.17	93.0

2.2.2 Fractured samples

Ten samples were tested: four OPA sandy, two COX clay-rich and four COX carbonate-rich. They were prepared to different sizes of diameter/length D/L = 50/(75 – 100) mm and 80/(280 – 300) mm. Their initial characteristics were determined before testing and are summarized in table 2.4. The grain densities of the OPA and COX samples are nearly

equal to 2.7 g/cm^3. The dry densities of the OPA sandy samples are slightly higher than that of the COX carbonate- and clay-rich ones. Due to the sampling and long storage durations of 1 – 2 years, the samples were desaturated to some low degrees.

As observed in situ at URLs Bure and Mont-Terri /ARM 14/ /DE 15/ /BOS 17/ /HAL 21/, drift excavation generated mostly tensile fractures near the opening walls, which are responsible for increased hydraulic conductivities. For laboratory testing, similar fractures were artificially created in most of the samples by tensile cracking and/or direct splitting. Figure 2.3 shows fracture patterns in the samples illustrated with some photos made before testing and computed tomography (CT) images made after testing. The CT-images represent only the situations of the dismantled samples after unloading.

Group 1: Three samples COX1-2 and OPA1 (D/L = 50/(75-100) mm) were inserted in rubber jackets and then cracked by Brazilian tensile loading along the sample length. A single major fracture was creased in each sample parallel or subparallel to the axis. The fracture apertures reached to ~1 mm. Some minor fissures appeared near the major one.

Group 2: Three (sub)parallel fractures were generated in two samples OPA2-3 (D/L = 50/90 mm) at distance of ~15 mm. A fracture in OPA2 was however inclined to the outside surface and did not cross the other end face. The fracture apertures reached to ~1 mm. In OPA4, a regular fracture was produced by cutting an aperture of 30 mm width and 2 mm opening through the length. The extremely high fracture densities in OPA2-3 and the single wide aperture in OPA4 do not or rarely appear in situ.

Group 3: Four large cores COX2/4-6 (D/L = 80/(280-300) mm) were taken for examining scale effect on fracture sealing. Fractures were created by pressing a steel wedge along the sample length, which caused several separate pieces with irregular shapes and surfaces. These pieces were then assembled in rubber jackets but could not be exactly matched together. The fracture patterns were very complex with various directions, apertures, densities, and connections, as shown by the CT-images of the samples after testing. Note that white flecks on the CT-images reflect the carbonates with high density, which are more distributed in the samples COX4-6 from the carbonate-rich unit than in COX2 from the transition unit.

Tab. 2.4 Basic characteristics of the prepared samples before fracturing

Lithological facies	Drilled core	Depth/ orientation	Sample number	Size D/L (mm)	Bulk density (g/cm^3)	Dry density (g/cm^3)	Porosity (%)	Water content (%)	Degree of saturation (%)
OPA sandy facies	BLT-A10		OPA1	50/75	2.487	2.445	9.4	1.72	44
	BDM-B9-9		OPA2	50/90	2.515	2.478	8.2	1.49	45
	DBM-B9-18		OPA3	50/90	2.563	2.532	6.2	1.22	50
	DBM-B9-29		OPA4	50/90	2.559	2.527	6.4	1.27	50
COX clay-rich unit	EST49093	-482m/V	COX1	50/100	2.383	2.262	16.2	5.35	75
COX transition unit	EST57262	-456m/V	COX2	80/298	2.400	2.291	15.1	4.76	72
COX carbonate-rich unit	EST51223	-444m/H	COX3	50/80	2.437	2.369	12.2	2.87	56
	EST52318	-437m/V	COX4	80/283	2.584	2.553	5.4	1.21	56
	EST52335	-445m/H	COX5	80/300	2.425	2.397	11.2	1.14	25
	EST52337	-445m/H	COX6	80/280	2.434	2.405	10.9	1.21	27

Generally, most of the created fractures with wide apertures of 1 – 2 mm and high connectivity levels exhibited a similar scale of the in situ macro-fractures near the rock walls but much larger than those microfractures in the deep areas of the EDZ in the ULRs Bure and Mont Terri /ARM 14/ /DE 15/ /BOS 17/ /HAL 21/. Moreover, the artificially created fractures in the samples are more intensively interconnected than the realistic fractures within the EDZ.

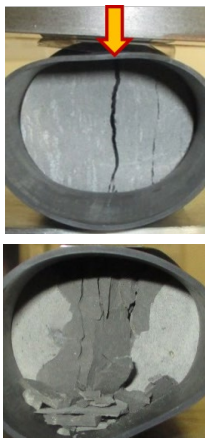

COX1
D/L= 50/100 mm

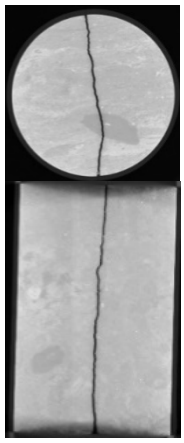

COX3
D/L= 50/80 mm

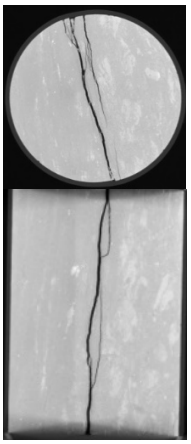

OPA1
D/L= 50/75 mm

a. group 1

OPA2
D/L= 50/90 mm

OPA3
D/L= 50/90 mm

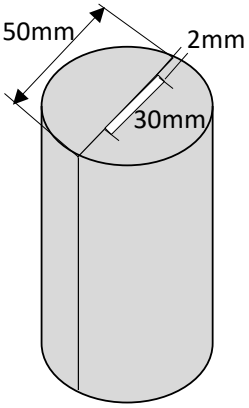

OPA4
D/L= 50/90 mm

b. group 2

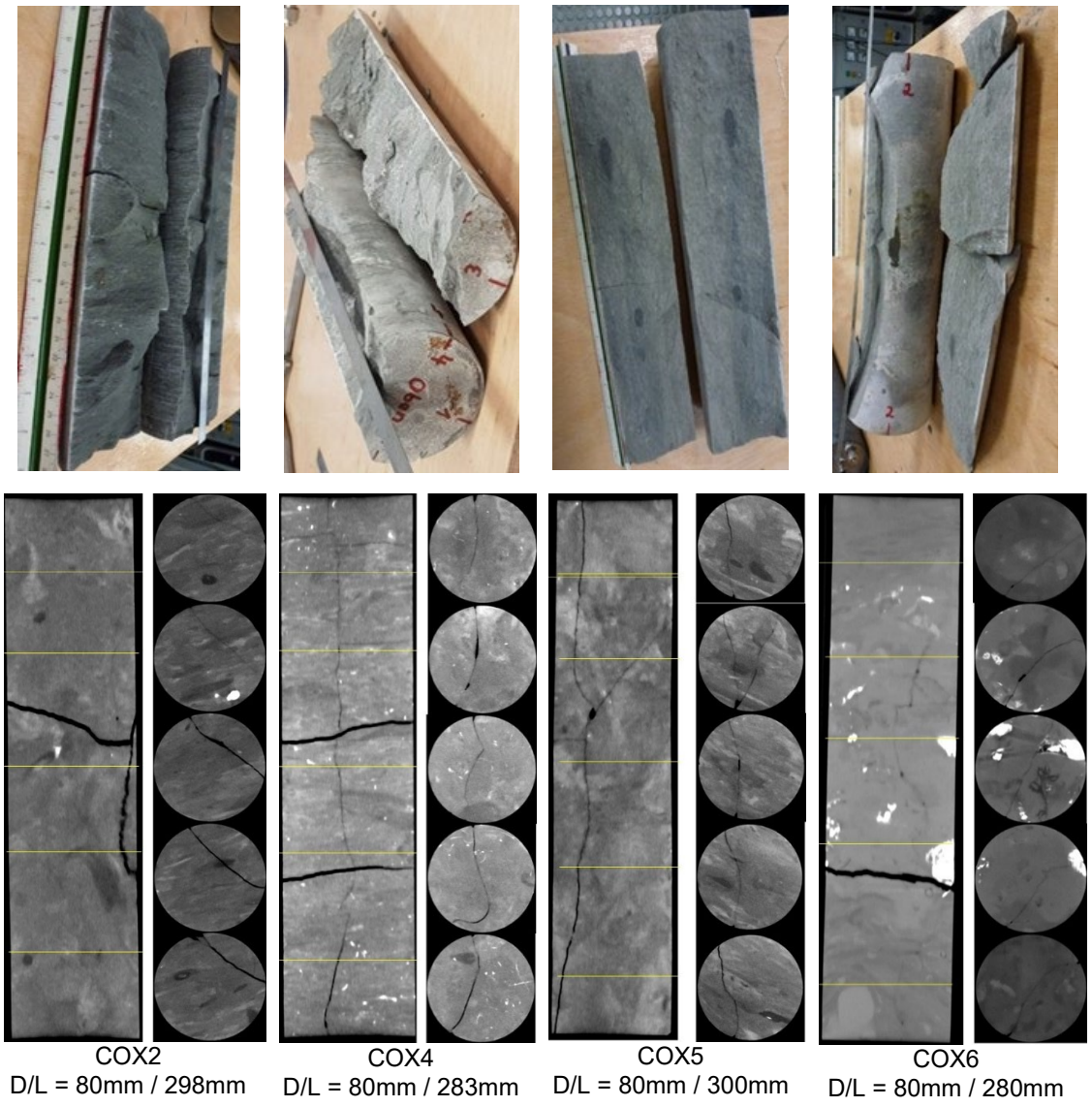

c. group 3

Fig. 2.4 Fracture patterns in the claystone samples illustrated with photos made before testing and CT-images after testing

3 Experimental methodology

3.1 Tests of the intact samples

A triaxial apparatus was upgraded with a new hydraulic system to determine water and gas conductivities of the intact claystone under the hydro-mechanical conditions of the rock mass. Figure 3.1 shows the test layout and setup. The apparatus allows a maximum radial stress (σ_r) of 70 MPa and a maximum axial stress (σ_a) of 200 MPa. The hydraulic system consists of two syringe pumps (Model 260D) and line connection elements. The pumps allow a maximum volume of 266 mL, a maximum pressure of 500 bar and flow rates in a range of 1 μL/min to 100 mL/min. The resolution of the pressure is about 0.1bar and the accuracy of the fluid volume measurement is better than ±0.5 .

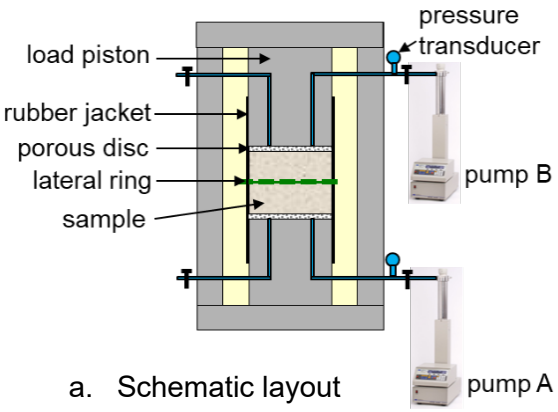

a. Schematic layout

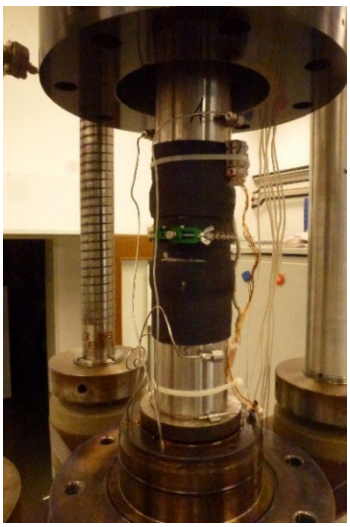

b. Sample installation

c. Testing machine

Fig. 3.1 Test layout and setup for measurements of water and gas conductivities of intact claystone under in situ hydro-mechanical conditions

A sample is inserted in a rubber jacket with a thickness of 2 mm. Sintered porous metallic discs and filter papers are placed at its top and bottom. The upper and lower load pistons were manufactured to a size of 70 mm diameter and 140 mm length. Two thin holes (D = 6 mm; L = 83 mm) drilled in the pistons serve to hydraulic connection between the sample and both pumps. In order to monitoring porewater pressure (or backpressure) in the sample, two pressure transducers are installed respectively at the inlet (P_{wi}) and outlet (P_{wo}) close to the sample. During mechanical loading, axial deformation (ε_a) is recorded by a linear variable differential transducer (LVDT) installed outside the cell, while radial strain (ε_r) is measured by a circumferential extensometer mounted around the sample outside the jacket. The volumetric strain is obtained approximately by $\varepsilon_v = \varepsilon_a + 2\varepsilon_r$. The testing apparatus is positioned in a large hall, where unfortunately the temperature could not be controlled but recorded at 23.0±2.5 °C during the tests.

Before testing, the system was calibrated using a steel cylinder of D/L = 70/50 mm and two porous metallic discs. The volume of the inlet (bottom) and outlet (top) reservoirs with the porous discs and lines connecting to the pumps were measured with water filling into them. The results are V_{in} = 11.75 cm^3 for the inlet and V_{out} = 11.30 cm^3 for the outlet.

To limit osmotic swelling of the samples, a synthetic porewater of COX formation was produced for use as permeant fluid. The main chemical components of the synthetic porewater are summarized in table 3.1, which are consistent with the COX porewater /AND 05/. The densities and viscosities of the synthetic water were measured at temperatures of 20 – 80 °C. The results are presented in figure 3.2 compared with the distilled water and the synthetic OPA porewater. It is obvious that the density and viscosity of the waters decrease with increasing temperature.

The rock stress state at the sampling position at the -490 m level of the URL Bure is characterized with a major horizontal component of σ_H = 16 MPa and a minor horizontal and vertical ones $\sigma_h \approx \sigma_v$ = 12.5 MPa /ARM 14/ /DE 15/. The mean stress $\sigma_m \approx$ 14 MPa and the in situ porewater pressure of P_w = 4.5 MPa were applied in the tests. Water permeability was measured under pressure differences of ΔP_w = 0.4 – 3 MPa, corresponding to hydraulic gradients of 1000 – 7500 m/m. Following the water flow testing, gas penetration testing was undertaken by helium gas at a controlled flow rate of 0.01 cm^3/min until breakthrough.

Tab. 3.1 Main chemical components of the synthetic COX and OPA water (in mmol/L)

Component	Na	Cl	Mg	Ca	SO4	K	Derived from
COX water	27.7	31.1	11.0	13.3	25.0	6.8	Andra (2005)
OPA water	24.0	30.0	16.9	25.8	14.1	1.6	Pearson (2003)

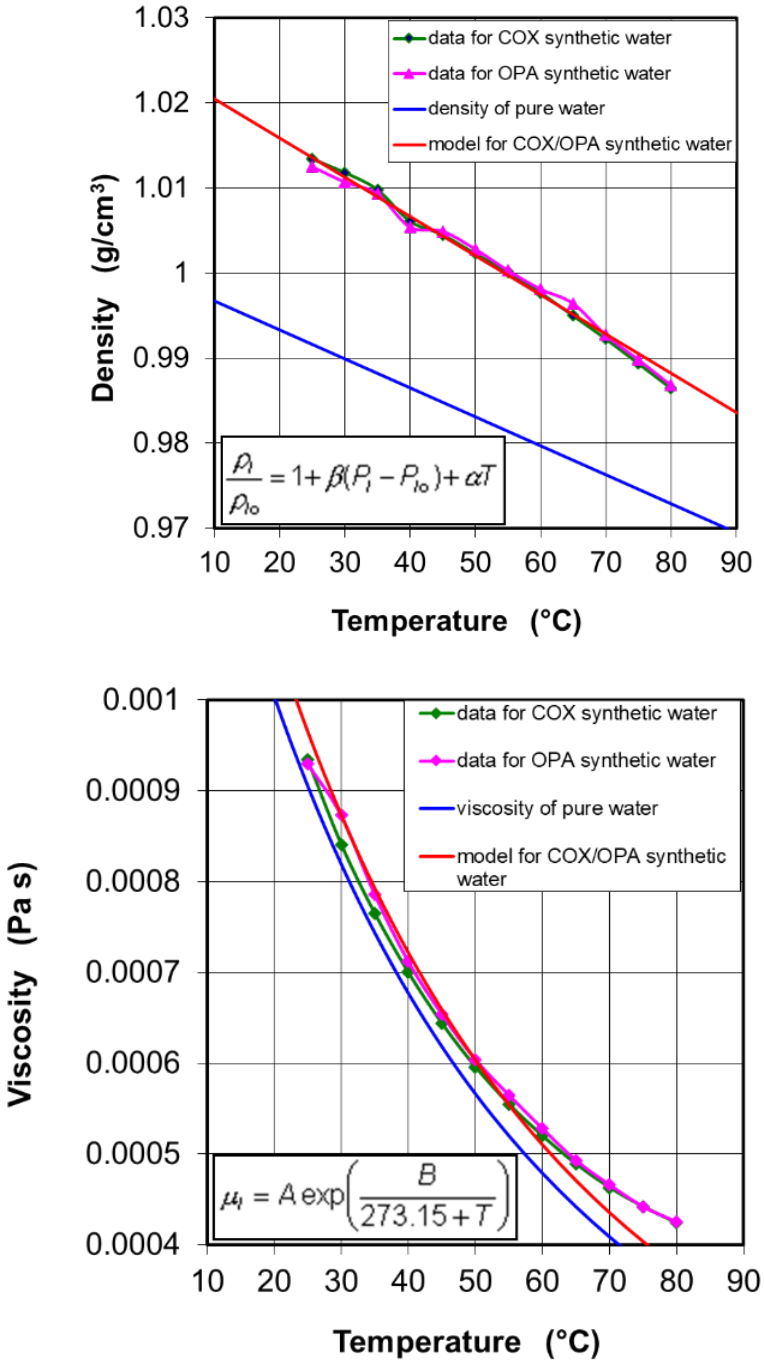

Fig. 3.2 Density and viscosity of the synthetic COX, OPA porewater and destilled water as a function of temperature

3.2 Tests of the fractured samples

3.2.1 Test setups

Two setups were developed and used for water and gas flow testing on the fractured claystone samples under mechanical compression. Figure 3.3 illustrate the layouts and apparatuses. The first setup (figure 3.3a) consists of three triaxial cells, which allow testing three samples of 50 mm diameter and 70 – 120 mm length in parallel under identical conditions. Axial and radial stress are controlled by two respective syringe pumps. One more pump is applied for injecting water or gas into the samples via inlet lines and sintered porous discs at bottom. The inlet pressure is measured by a pressure transducer for each sample. The fluid outflow is recorded at the top of each sample using a scaled burette at atmospheric pressure. Deformation of each sample is recorded axially by a LVDT installed at the top of the cell and laterally by a circumferential extensometer mounted at the middle of the length. The fractured samples in group 1 and 2 (figures 2.4a-b) were tested in this setup.

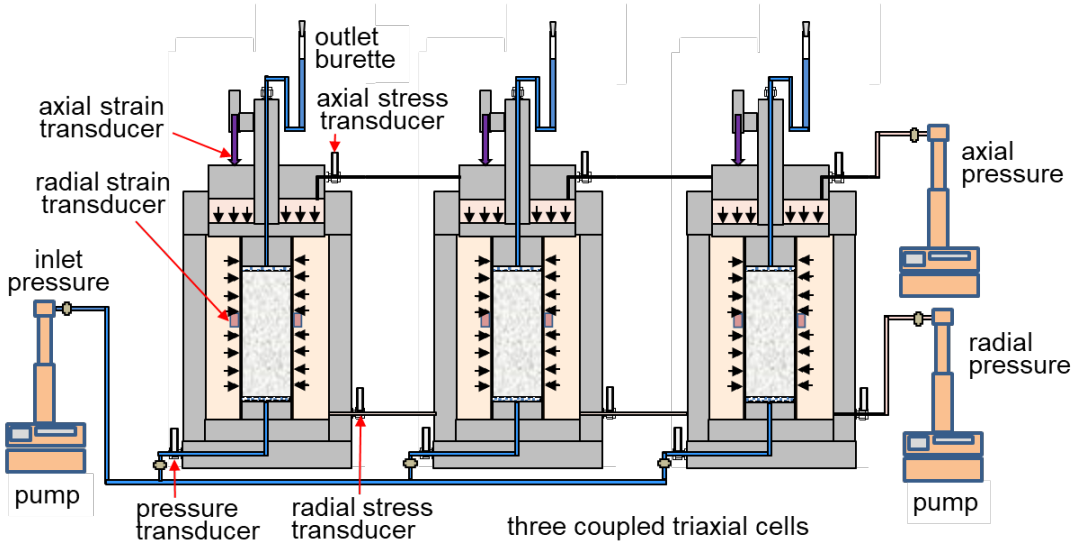

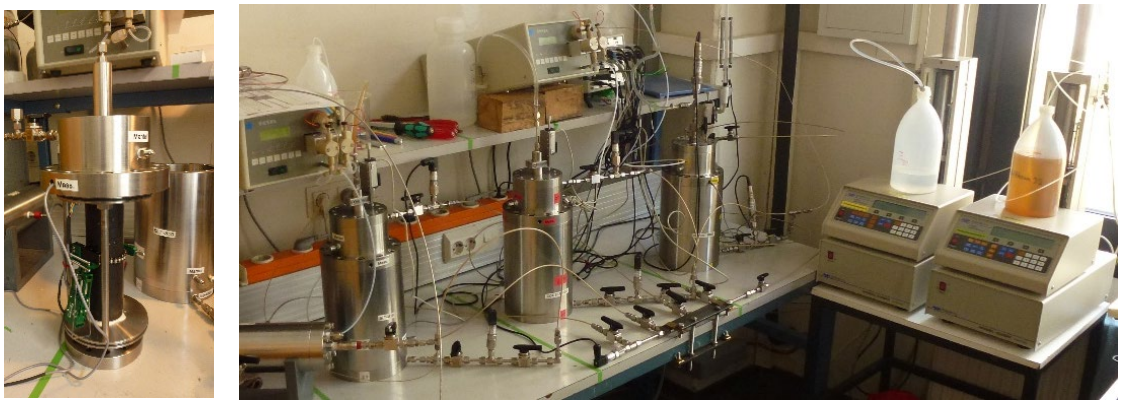

a. three parallel tests in coupled triaxial cells under identical conditions

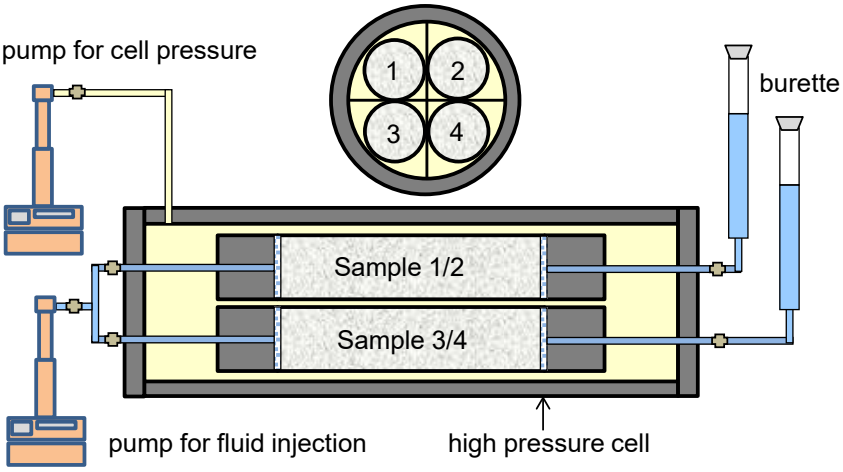

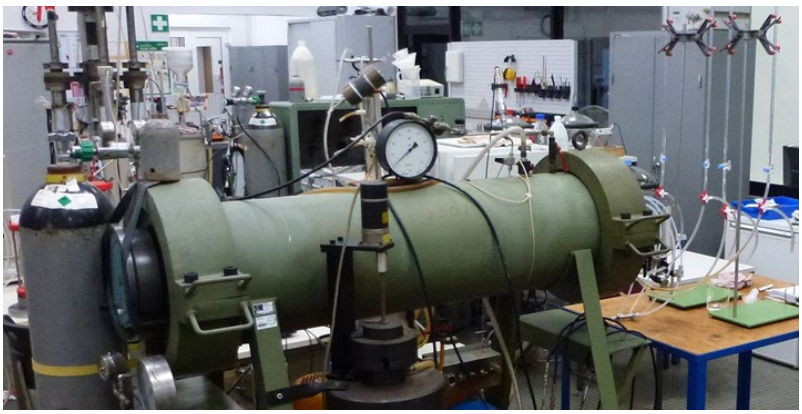

b. four parallel tests in a pressure vessel under identical conditions

Fig. 3.3 Two setups used for water and gas testing on fractured claystone samples

Four large samples in group 3 (figure 2.4c) were tested in a pressure vessel (figure 3.3b) allowing a maximum pressure of 25 MPa. Each sample is inserted in a rubber jacket and covered by two sintered porous discs and two pistons. A same confining stress is applied to the samples by a pressure/volume GDS-controller. The water or gas injection is controlled by means of a syringe pump. The fluid outflow is recorded at the outlet of each sample using a burette at atmospheric pressure.

3.2.2 Test procedure

These specific setups make it possible to test the fractured samples in parallel by application of the dynamic EDZ conditions in acceptable time periods. A common test procedure was designed and performed sequentially in the following steps: a) reconsolidation and water flow under effects of rock stress and porewater pressure; b) subsequent gas generation and migration through sealed fractures; and c) resealing of gas-induced pathways after gas escape.

I. The reconsolidation and water permeability changes of the fractured samples were determined by injecting synthetic water into them under multistep increased stresses. Synthetic COX and OPA porewaters were injected into the respective COX and OPA samples. The hydrostatic stress σ was stepwise increased up to 10 MPa for the samples of group 1, 13 MPa for group 2, and 4 MPa for group 3, respectively. The stress range of 10-13 MPa selected for groups 1-2 covers the lithostatic stresses surrounding the potential repository at a depth of ~500 m below the ground surface. The application of the low stress of 4 MPa to group 3 is to examine impact of swelling pressure of a draft/shaft seal on the EDZ. Each step lasted for 1 to 4 months. The water injection pressure P_{wi} was adjusted in a range of 0.1 – 1.0 MPa much below the confining stresses to avoid hydraulic fracturing. During steady-state water flow, apparent water permeability was determined according to Darcy's law for incompressible fluids /HOR 96/:

$$K_{\mathrm{w}} = \frac{Q_{\mathrm{w}}\,\mu_{\mathrm{w}}\,L}{A\,(P_{\mathrm{wi}} - P_{\mathrm{wo}})} \tag{3.1}$$

where K_w is the water permeability (m^2), Q_w is the water flow rate (m^3/s), μ_w is the dynamic viscosity of the water (0.95×10^{-3} Pa·s for both the COX and OPA water), L is the sample length (m), A is the cross section of the sample (m^2), P_{wi} and P_{wo} are the inlet and outlet water pressure (Pa), respectively.

II. Gas flow testing followed at the last load step by injecting helium gas into the water-saturated and fracture-sealed samples. Before gas injection, an attempt was made to remove the water remained in the inlet and outlet reservoirs. The gas injection pressure P_g was stepwise increased at small increments of 0.1 – 0.2 MPa per day. As first gas bubbles were detected at the outlet side, the gas pressure in the inlet was defined as the breakthrough pressure P_b. Beyond that, the gas injection continued for determination of apparent gas permeability according to Darcy's law for compressible fluids /ROD 03/:

$$K_{\mathrm{g}} = \frac{2\,Q_{\mathrm{g}}\,\mu_{\mathrm{g}}\,P_{\mathrm{go}}\,L}{A\left(P_{\mathrm{gi}}^2 - P_{\mathrm{go}}^2\right)} \tag{3.2}$$

where K_g is the gas permeability (m^2), Q_g is the gas outflow rate (m^3/s), ν_g is the dynamic viscosity of helium gas (1.96×10^{-5} Pa·s), P_{gi} and Pg_o are the inlet and outlet gas pressure (Pa), respectively.

III. Resealing of the gas-induced pathways was examined by measuring water permeability, which is compared with that before gas penetration.

4 Results and discussion

4.1 Results from the intact samples

4.1.1 Water permeability

Sample COX-EST58148 was prepared to a size of D/L = 70/40 mm and fully saturated. Its basic properties are summarized in table 2.3. The test on this sample focused on determination of its water permeability under a hydrostatic stress of 14 MPa and a mean porewater pressure of 4.5 MPa (corresponding to the rock conditions at the sampling position at URL Bure). The conditions were applied sequentially in several steps. Figure 4.1 depicts the evolution of applied hydrostatic stress (σ), water pressure in the inlet (P_{wi}) and outlet (P_{wo}), and resulting axial and radial strain (ε_a, ε_r), and accumulated water volume measured in the inlet and outlet (V_{wi}, V_{wo}).

I. Consolidation

The sample was firstly reconsolidated in drained condition without contacting water. A hydrostatic load was applied at a load rate of $5 \cdot 10^{-4}$ MPa/s up to 9.5 MPa, being equivalent to the “effective” mean stress of the clay rock at the sampling position. The loading led to a compression in axial and radial directions. The relatively higher axial strain might be due to unperfected assembly of the sample, porous discs and load pistons. The applied load was kept for a period of about 3 days to reconsolidate the micro-fissures created by sampling. Then an unloading/reloading cycle was performed at the same load rate down to 1 MPa and up to 9.5 MPa again. From the reloading path, a bulk modulus is obtained to $E_v = \Delta\sigma / \Delta\varepsilon_v = 55$ GPa.

II. Water injection

Keeping the stress constant, the synthetic water was injected into the inlet and outlet reservoirs at a unique pressure of $P_{wi} = P_{wo} = 0.7$ MPa. Then both the inlet and outlet were switched off. Whereas P_{wo} rose gradually with time, P_{wi} fell slightly and then turn over to rising. The water pressures at both sides reached to a same value of 3.0 MPa at day 20. During the saturation phase, a gradual swelling occurred in axial and radial directions (figure 4.1a). The axial and radial swelling strains are quite similar $\Delta\varepsilon_a \approx \Delta\varepsilon_r \approx$

-0.04 %. The swelling of the sample might compress the water in the porous discs and increase the inlet and outlet pressures in the shut-off conditions.

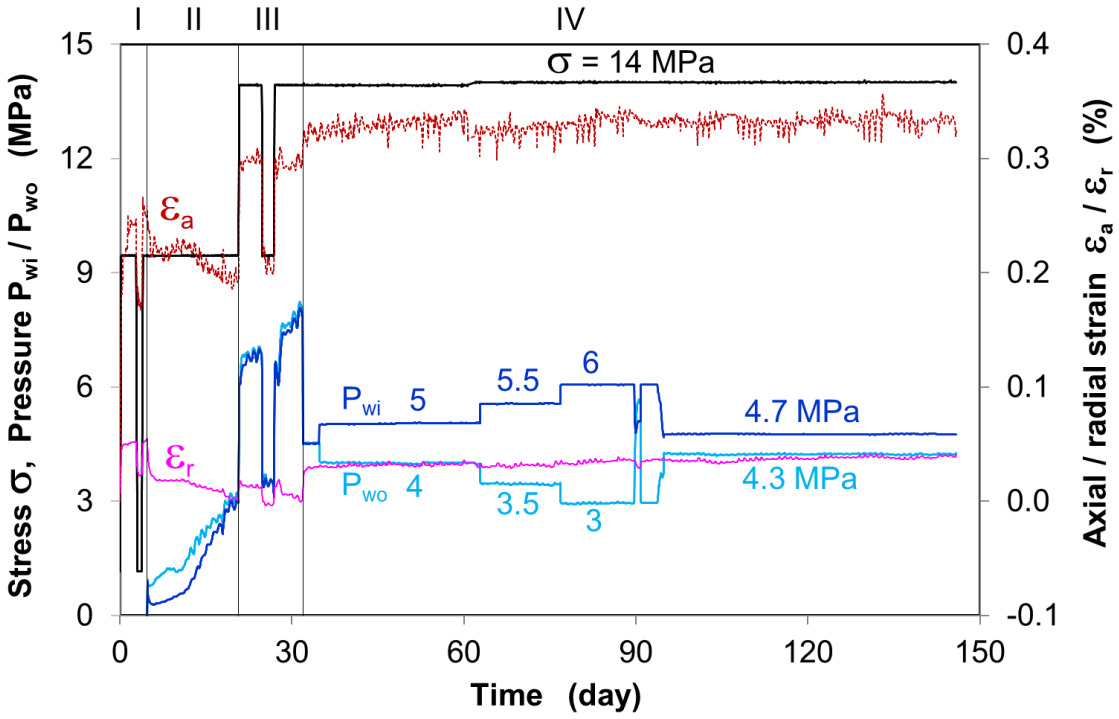

a. applied confing stress, in-/outlet pressures, and resulting axial/radial strains

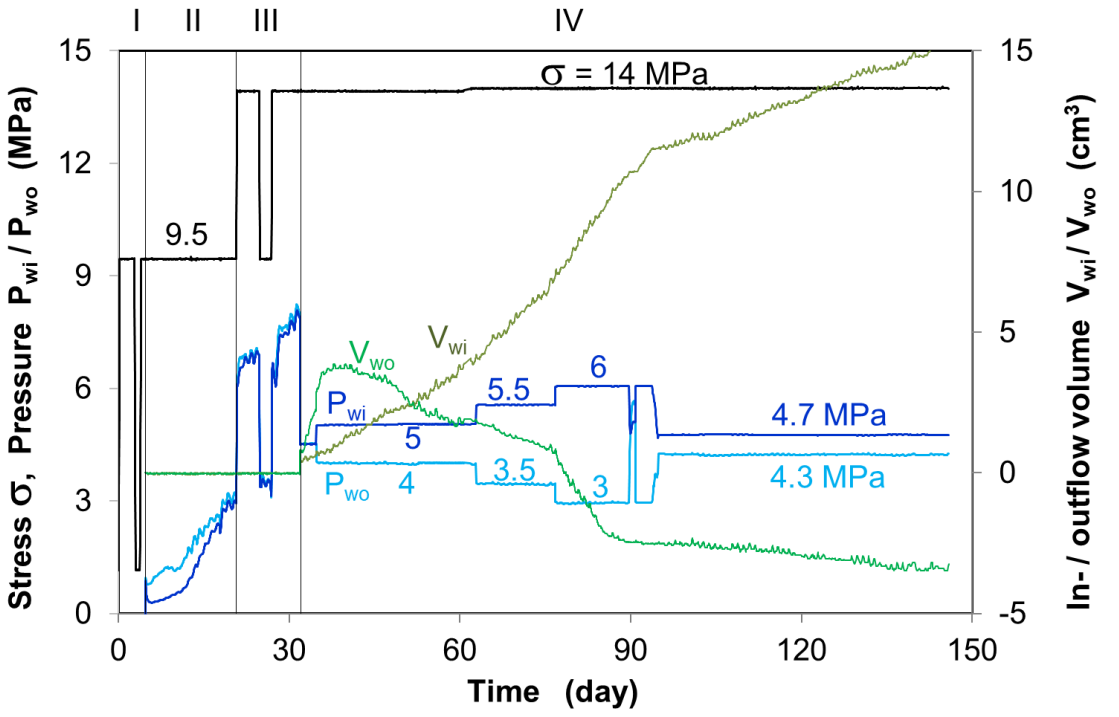

b. water flow recorded in inlet and outlet

Fig. 4.1 Results obtained on the intact claystone sample COX-EST58148

III. Reconsolidation

In order to compensate the swelling, the confining stress was increased to 14 MPa in the undrained condition. The stress increase caused a rapid increase of the backpressures up to $P_{wi} \approx P_{wo}$ = 6.0 MPa and then to 7.0 MPa over 5 days. These data with $\Delta\sigma$ = 14.0 – 9.5 = 4.5 MPa and ΔP_w (= $\Delta P_{wi} = \Delta P_{wo}$) = 7.0 – 3.0 = 4.0 MPa yield Skempton's pore pressure coefficient $B = \Delta P_w/\Delta\sigma$ = 0.89. Subsequently, an unloading/reloading cycle was performed in the range of σ = 9.5 to 14.0 MPa. The unloading led to a decrease in the backpressures down to 3.5 MPa, yielding B = 0.81. The reloading led to a gradual increase in the backpressures to 8.0 MPa over 6 days, yielding B = 1.0. This value suggests full water saturation of the sample.

IV. Measurement of water permeability

First, the backpressures were adjusted to the *in situ* porewater pressure of 4.5 MPa by reducing the increased pressures. This resulted in a rapid axial compression of $\Delta\varepsilon_a$ = 0.035 % and radial one of $\Delta\varepsilon_r$ = 0.025 % (figure 4.1a). Then water inflow was observed into both the inlet and outlet by volume increase of ΔV_{wi} = 0.56 cm^3 and ΔV_{wo} = 2.25 cm^3 over 3 days (figure 4.1b). This phenomenon cannot be yet reasonablly interpreted. Water permeability was measured at four hydraulic gradients by keeping the mean pore pressure of 4.5 MPa:

a. In the first phase over 4 weeks, the inlet pressure P_{wi} was increased to 5 MPa while the outlet pressure P_{wo} decreased to 4 MPa. The resulting pressure difference is ΔP_w = 1 MPa, corresponding to a hydraulic gradient of i = 2500.
b. In the second phase over 2 weeks, the backpressures were adjusted to P_{wi} = 5.5 MPa and P_{wo} = 3.5 MPa, ΔP_w = 2 MPa (i = 5000).
c. In the third phase over 2 weeks, P_{wi} = 6 MPa and P_{wo} = 3 MPa were applied, ΔP_w = 3 MPa (i = 7500). Following that, the in- and outlet were switched off for 1 day and then the previous pressures were adjusted again.
d. In the final phase, a low pressure gradient of ΔP_w = 0.4 MPa (i = 1000) was applied by P_{wi} = 4.7 MPa and P_{wo} = 4.3 MPa for a longer duration of 1.5 months.

During each water injection phase, the water volume accumulated at inlet V_{wi} and outlet V_{wo} were recorded. Figure 4.1b shows that both V_{wi} and V_{wo} increase almost linearly with time. However, inflow rate is slightly higher than the outflow one at each step, due to a minor leakage of the inlet reservoir (detected after testing). From the linear parts of

V_{wi}–t and V_{wo}–t curves during each flow phase, apparent water permeability can be obtained according to Darcy's law (equation 2.7). The measured data are summarized in table 4.1. The data indicate no dependency of the water permeability on the applied pressure gradients. The average value of K_{wo} = 8x10^{-21} m^2 obtained from the outflow is reasonable for the true water permeability of the sample, while K_{wi} = 1.4x10^{-20} m^2 from the inflow is too high due to the leakage of the inlet.

Tab. 4.1 Water permeabilities obtained from the stationary inflow and outflow through the sample at different pressure gradients

Pressure gradient ΔP_w (MPa)	Test duration Δt (day)	Inflow volume V_{wi} (cm^3)	Permeability from inflow K_{wi} (m^2)	Outflow volume V_{wo} (cm^3)	Permeability from outflow K_{wo} (m^2)
1	8	0.32	$1.3 \cdot 10^{-20}$	0.83	$1.1 \cdot 10^{-20}$
2	12	2.32	$1.1 \cdot 10^{-20}$	0.91	$5.3 \cdot 10^{-21}$
3	6	1.51	$1.2 \cdot 10^{-20}$	1.38	$1.0 \cdot 10^{-20}$
0.4	34	2.52	$2.1 \cdot 10^{-20}$	0.77	$6.1 \cdot 10^{-21}$
Mean value			$1.4 \cdot 10^{-20}$		$8.0 \cdot 10^{-21}$

Sample COX-EST60765 was prepared to a size of D/L = 70/50 mm and not fully saturated. Its characteristics are given in table 2.3. The test on it aimed at determining water permeability, gas penetration and resealing of gas-induced pathways under a hydrostatic stress of 14 MPa and a mean porewater pressure of 4.5 MPa. The test was performed in four sequential steps with (I) reconsolidation and resaturation; (II) measurement of water permeability; (III) gas penetration testing; and (IV) examination of re-sealing of gas-induced fractures. The total test evolution is illustrated in figure 4.2. Results of the gas testing will be presented later in next section 4.2.

I. Reconsolidation

The sample was reconsolidated and resaturated under hydrostatic stress of σ = 9.5 MPa and injection of the synthetic water at in-/outlet pressure of P_{wi} = P_{wo} = 0 and 1.5 MPa for a total duration of 7 days. The first load phase at zero water pressure over 1.6 days caused a compression to an axial strain of ε_a = 0.29 %, a radial strain of ε_r = 0.25 %, and a volumetric strain of ε_v = 0.79 %. The volume reduction decreased the porosity from 17.3 % to 16.2 % and thus increased the degree of water saturation from 92.5 % to 100 %, as shown in figure 4.3. The subsequent water injection at pressure to 1.5 MPa did not cause significant deformation.

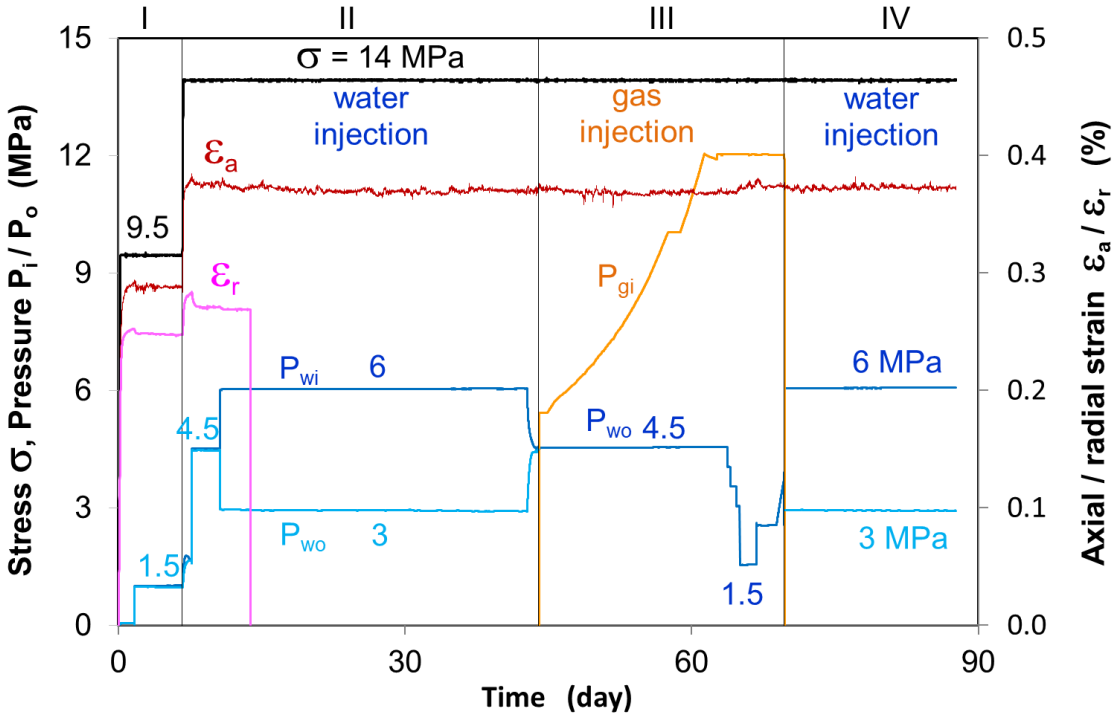

a. applied confing stress, in-/outlet pressures, and resulting axial/radial strains

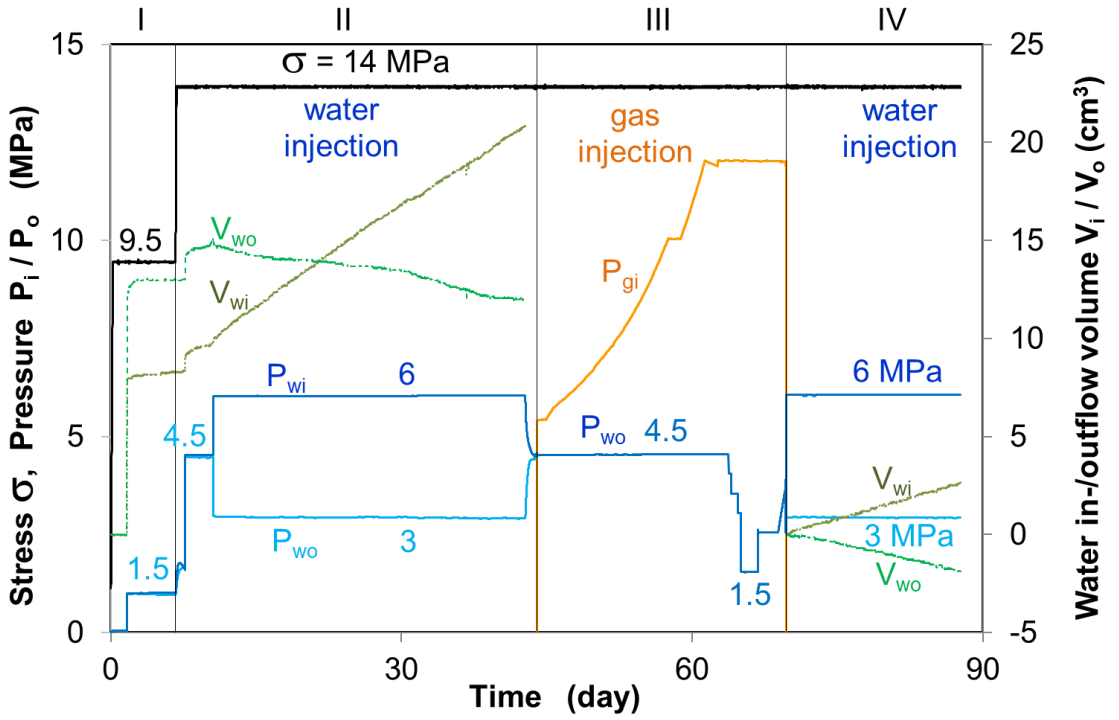

b. water flow recorded in inlet and outlet

Fig. 4.2 Results obtained on the intact claystone sample COX-EST60765

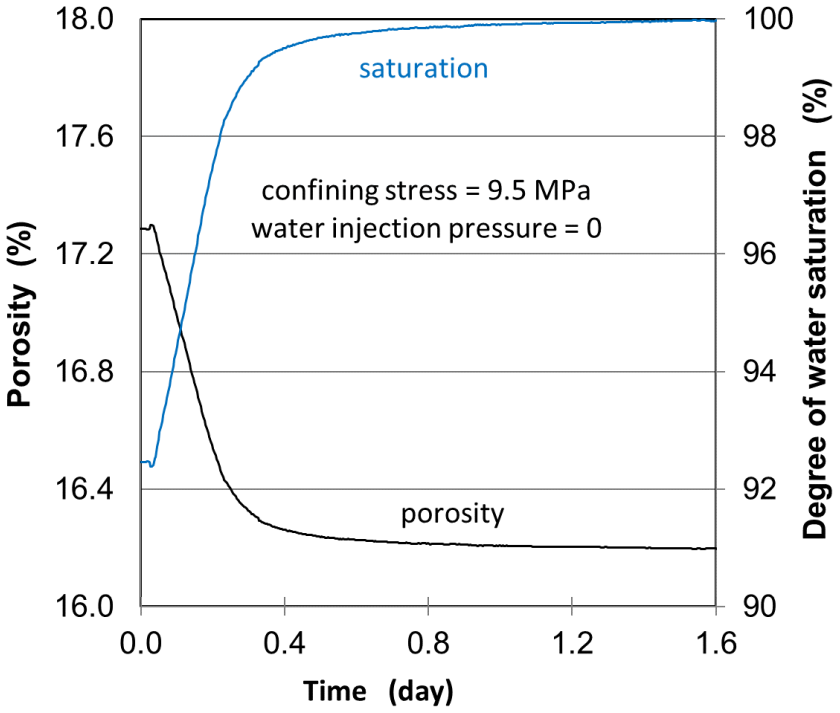

Fig. 4.3 Evolution of porosity and water saturation of the sample during reconsolidation

II. Measurement of water permeability

In the first, the hydrostatic stress was increased to 14 MPa, which caused compressive strains to ε_a = 0.37 %, ε_r = 0.28 % and ε_v = 0.93 %. The corresponding porosity is about 16 %. Secondly, the water pressures in inlet and outlet were increased to 4.5 MPa, which yielded a small expansion of $\Delta\varepsilon_a$ = -0.007 %, $\Delta\varepsilon_r$ = -0.01 % and $\Delta\varepsilon_v$ = -0.027 % over 3 days. Keeping the mean porewater pressure of 4.5 MPa, the inlet and outlet pressure were adjusted to P_{wi} = 6 MPa and P_{wo} = 3 MPa, respectively. Under the pressure difference of ΔP_w = 3 MPa (i = 7500), the volume of water inflow V_{wi} and out flow V_{wo} were monitored for a month. Both increased linearly with time, but the inflow rate is higher than the outflow one due to the minor leakage of the inlet. Therefore, the water permeability was determined from the outflow to a value $K_{wo} = 4x10^{-21}$ m^2, a half of the value of the first sample COX-EST58148.

The water permeability values of $4x10^{-21}$ to $8x10^{-21}$ m^2 obtained on the intact COX samples under the hydrostatic stress of 14 MPa and porewater pressure of 4.5 MPa are consistent with those of $1x10^{-20}$ to $1x10^{-21}$ m^2 obtained on two COX samples in oedometer cells (D/L = 50/10 mm) /ZHA 13b/.

4.1.2 Gas penetration and resealing of gas pathways

Following the water flow testing, gas penetration testing was undertaken to determine gas migration properties of the intact sample under the *in-situ* stress and porewater pressure conditions (step III). In the first, the water in the inlet reservoir was removed by vacuum pumping, while the water backpressure of P_{wo} = 4.5 MPa at the opposite side was kept. Helium gas was then injected into the inlet reservoir at a high pressure of P_{gi} = 5.3 MPa for a day. No remarkable response of the axial strain appeared (figure 4.2a), while the measurement of radial strain failed before.

Subsequently, the gas was injected at a controlled flow rate of 0.01 cm^3/min up to a pressure of 10 MPa, which took 12 days, as shown in figure 4.4. The maximum pressure was then kept for another day. During the gas injection, very negligible small outflow rates were recorded to be below $3 \cdot 10^{-12}$ cm^3/s, which was predominantly induced by gas diffusion and the data noise was resulted from the fluctuation of uncontrolled room temperature. That means no advective gas flow took place.

The gas injection continued at the same rate up to a high pressure of 12 MPa, at which the injection pump was switched off. Just at this point, the gas outflow rate increased rapidly, indicating a breakthrough event. Obviously, the high gas pressure generated micro-fissures forming a network spanning both the ends of the sample. This injection pressure is defined as the gas breakthrough pressure, P_b = 12 MPa. The subsequent shut-down of the gas injection led to a slow declination of the pressure to 11.9 MPa over a day. This is due to the continual outflow of the residual gas in the pathways with slowed rates. However, the pathways tended to seal with a rapid reduction of the gas outflow to zero ($Q_g < 10^{-12}$ cm^3/s). The sealing of the network might be attributed to combined impact of consolidation of the gas-occupied micro-fissures under the increased effective stress and water resaturation of the fissures at the outlet side due to the reduction of the inner gas pressure.

According to /HAR 17/, the gas pressure declined to termination of flow can be referred to the apparent capillary threshold of the pathway at the downstream end of the sample, defined as $P_{co} = P_{go} - P_{wo}$, where P_{go} is the gas pressure at the sample end. Assuming the pressure of the residual gas being the same along the pathways, $P_{gi} = P_{go}$, the apparent capillary threshold can be estimated to be P_{co} = 11.9 – 4.5 = 7.4 MPa.

When the gas pressure was increased again to the same level as the breakthrough pressure that had induced the pathways, no gas outflow could be detected over a day, indicating a complete closure of the pathways. To reopen the pathways, the capillary pressure was increased to 8 MPa by decreasing the water backpressure down to P_{co} = 12 – 8 = 4 MPa, which yielded a jump of the gas outflow rate by an order of magnitude. Further increasing the capillary pressure by reducing P_{wo} to 3.5, 3 and 1.5 MPa accelerated the gas flow. Particularly during the last phase at P_{wo} = 1.5 MPa, the acceleration of the gas flow was very significant. It seems that new micro-fissures were created by decreasing the water backpressure or by increasing the capillary pressure. In contrast, the increase of the water backpressure to P_{wo} = 2.5 MPa slowed the gas flow. When the gas injection was terminated, the residual gas still flowed into the outlet reservoir and rose the outlet (water + gas) pressure again.

Assuming the gas outlet pressure P_{go} is equivalent to the water backpressure P_{wo}, one can calculate apparent gas permeability K_g according to equation (8). Figure 4.5 shows the evolution of the apparent gas permeability. The K_g-value increases with decreasing the outlet pressure $P_{co} = P_{wo}$ or increasing the pressure gradient $\Delta P_g = P_{gi} – P_{wo}$.

In order to examine re-sealing of gas pressure-induced pathways, a second measurement of water permeability was measured again by injecting the synthetic water at the same pressure as before. The measured water inflow (V_{wi}) and outflow (V_{wo}) are illustrated in figure 4.2b, based on which the water permeability is calculated according to equation (7). Two similar values are obtained: $K_{wi} = 7x10^{-21}$ m^2 from the inflow and $K_{wo} = 5x10^{-21}$ m^2 from the outflow. They are very close to that measured before the gas penetration. Obviously, the gas-induced pathway can reseal completely under the combined impact of mechanical load and water-induced clay swelling.

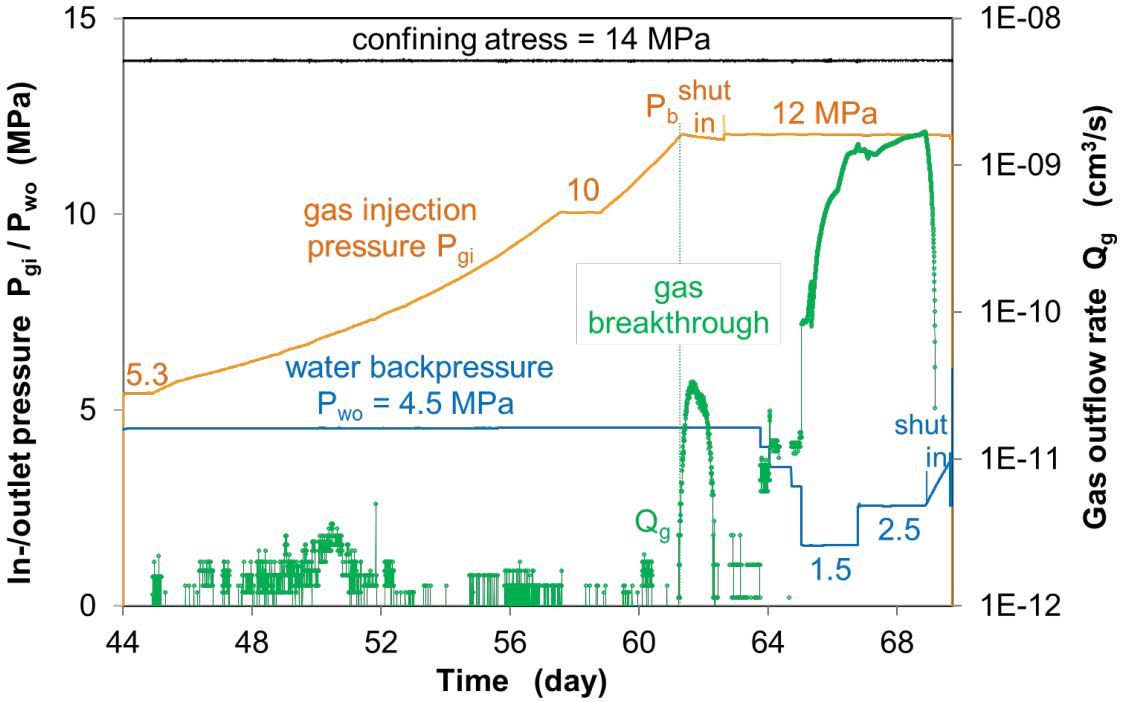

Fig. 4.4 Results of the gas penetration testing on the intact and water-saturated claystone sample COX-EST60765

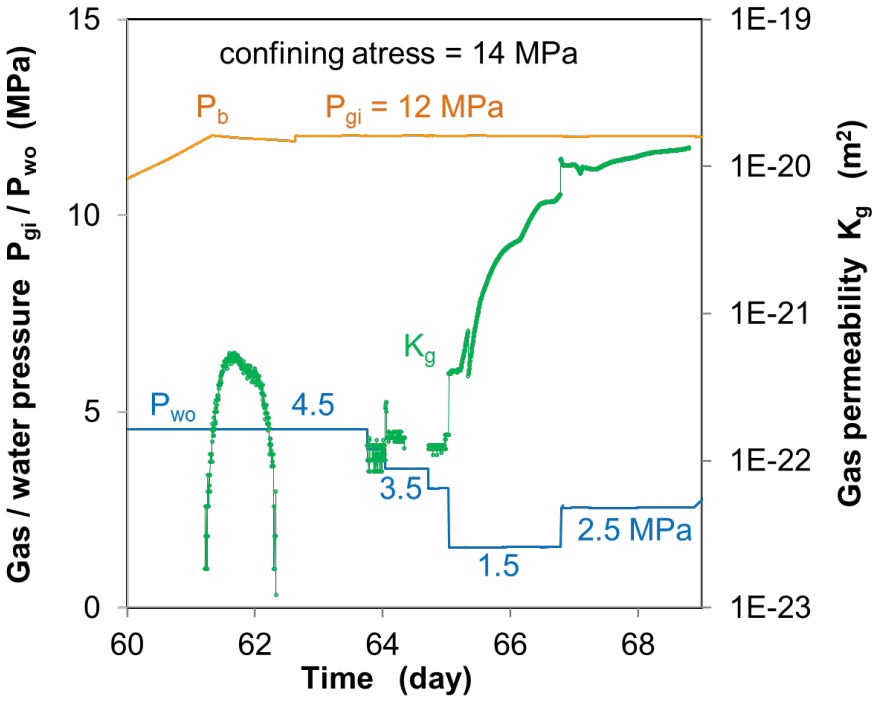

Fig. 4.5 Evolution of the apparent gas permeability measured after gas penetration through the intact sample COX-EST60765

4.2 Results from the fractured samples

4.2.1 Fracture closure and permeability change

4.2.1.1 Fracture closure

The fracture closure was measured by radial strain ε_r (sub)normal to the fracture planes along the sample length. Figure 4.6 shows the typical process of fracture closure obtained on two fractured samples OPA2/4 during water flow under multistep increased stresses, together with axial strain ε_a parallel to the fracture planes and water permeability K_w in axial direction. As already shown in figure 2.4b, OPA2 consisted of three axially (sub)parallel fractures with apertures of ~1 mm and at distance of ~15 mm; and OPA4 had a regular fracture geometry with a length of 30 mm and a wide aperture of 2 mm along the axis.

Firstly, a low hydrostatic stress of 0.5 MPa was applied without water injection to stabilize the fracture structure. Over a month, the fractures closed with time to ε_r = 0.1 % at OPA2 and ε_r = 0.04 % at OPA4, respectively. The closure of the regular fracture in OPA4 is very limited because of the strong resistance of the wide pillars on both end sides. In contrast, the closure of the irregular fractures in OPA2 is larger due to effect of high stress concentrations on smaller contacting areas between the rough fracture walls.

As the synthetic water was injected into the fractures, a rapid swelling took place in all directions to strains of $\varepsilon_a \approx \varepsilon_r \approx 0.2$ % at OPA2 and 0.3 % at OPA4, respectively. The radial swelling observed externally indicates high local swelling pressures acting in contact areas between rough fracture surfaces, which excess the external stress. Moreover, the fracture walls expanded into the non-stressed interstices. This was demonstrated by submerging a fractured discs in the synthetic water without mechanical loading (figures 4.7 a-b). The initial fracture opening of 2 mm was quickly filled by swelling of the fracture walls as contacting water. The filling material became mud with low density and can be easily compacted under stress (figure 4.7c). The subsequent increase of the hydrostatic stress to 2, 3, 4, 6, and 10 MPa resulted in more normal compaction compared to the parallel one, $\varepsilon_r \approx 2\,\varepsilon_a$. Under each constant stress, the strains evolved gradually with decreased rates until stabilization. In correspondence with the compaction over a long period of 1.7 years, the water permeability decreased significantly by three to four orders of magnitude to low values of 9×10^{-20} m^2 at OPA2 and 1×10^{-17} m^2 at OPA4, respectively.

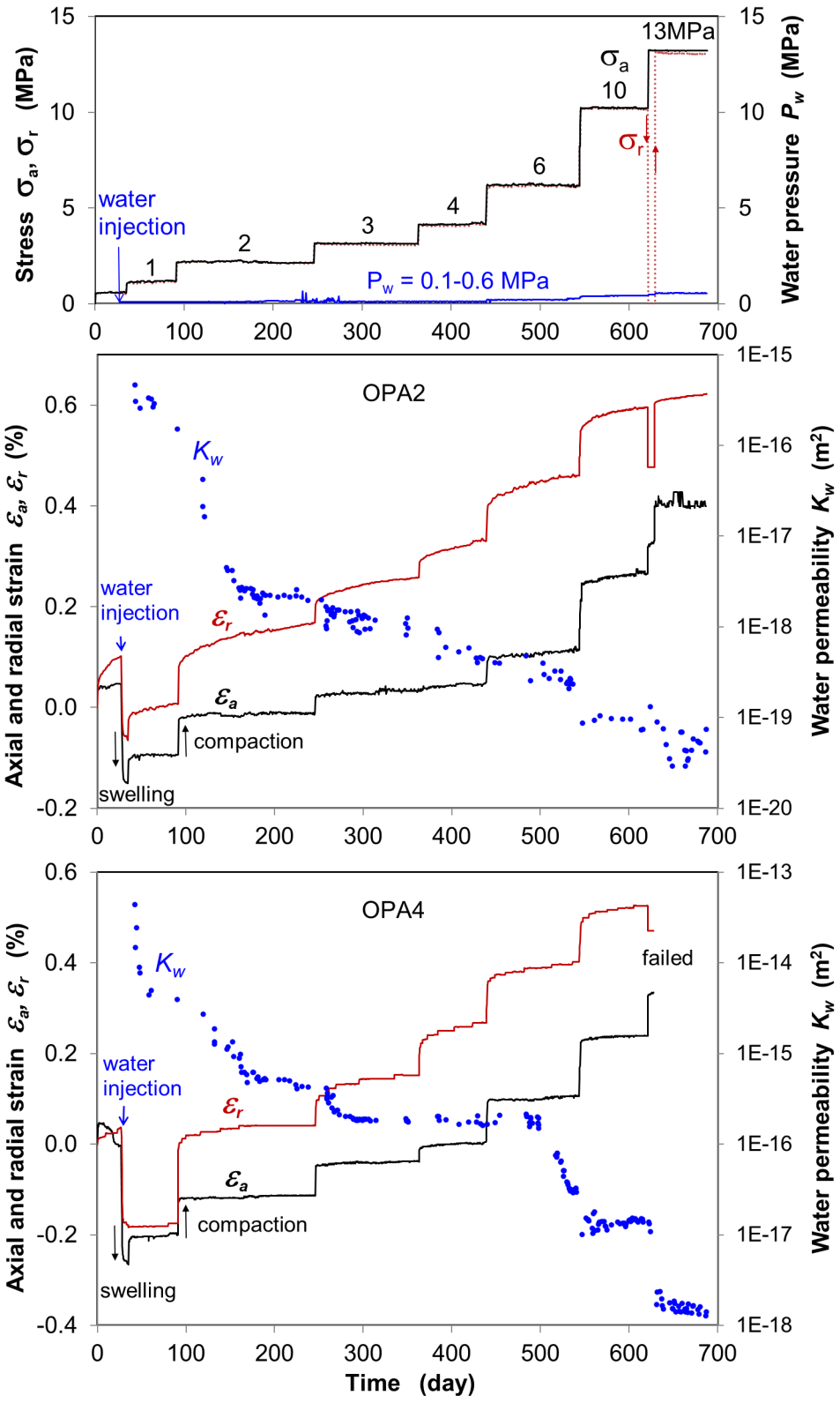

Fig. 4.6 Evolution of axial/radial strains and water permeability obtained on the fractured sandy claystone samples OPA2 with three subparallel fractures and OPA4 with a regular fracture during water flow under stresses

In order to examine shearing effect on the fracture sealing, a deviatoric stress was applied by decreasing the radial stress to zero and increasing the axial stress to 13 MPa, $\sigma_a - \sigma_r$ = 13 MPa. This caused shear fractures inclined to the axis at angles of 30° – 35° (figure 4.7d). The relative shear movements of the separated matrixes disconnected the filled fractures partly. Figure 4.7e sketches the combined effects of local normal compaction to close fracture aperture, shear deformation to disconnect fracture network, and clay swelling/slaking to seal fracture void.

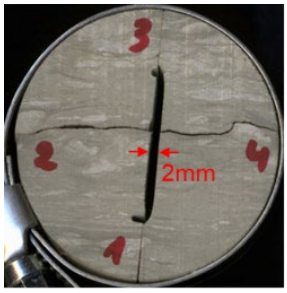

a. a fracture of 2 mm opening in a sandy claystone sample OPA4

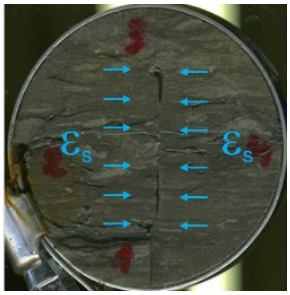

b. filling of the fracture by water-induced swelling/ slaking of fracture walls

c. normal compaction of the fracture under hydrostatic stress

OPA2

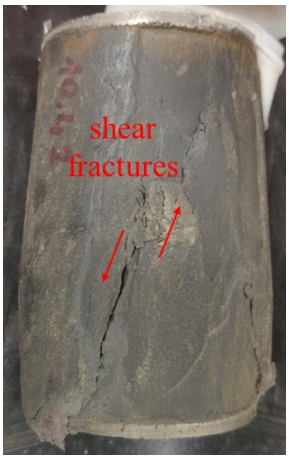

OPA4

d. shear fractures generated at a deviatoric stress of 13 MPa

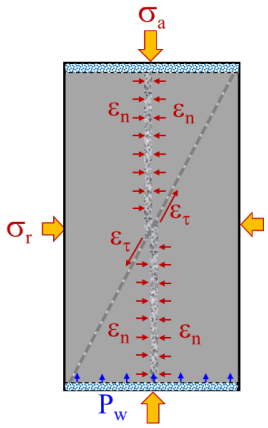

Sketch

e. effects of normal/shear strains and clay swelling on fracture sealing

Fig. 4.7 Fracture sealing observed in the OPA sandy claystone samples under combined effects of water-induced swelling/slaking (ε_s), local normal and shear deformation (ε_n, ε_t) under hydrostatic and shear stresses

4.2.1.2 Water permeability

As a key parameter of fracture sealing, water permeability of each fractured sample was measured during water injection under increased stresses. The results are depicted in figure 4.8 for all the samples.

Initially, the permeabilities of the fractured samples were determined by gas injection at a pressure of 0.03 MPa and under the low stresses of 1 MPa for groups 2/3 and 2 MPa for group 1. High gas permeability values were obtained to 10^{-13} – 10^{-12} m^2 for all the samples. As soon as the water was supplied, the fracture walls were wetted and expanded into the interstices and clogged the pathways (figure 4.7b). This decreased the permeability tremendously by several orders of magnitude to values of 10^{-18} – 10^{-17} m^2 at the clay-rich samples COX1-2, 10^{-16} – 10^{-14} m^2 at the sandy ones OPA1-4, and 10^{-15} – 10^{-13} m^2 at the carbonate-rich ones COX3-6. The permeability reduction continued with time to lower values of 10^{-18} – 10^{-17} m^2 within 1 – 2 months at most of the samples. However, the carbonate-rich sample COX3 with a low clay content of 21 % and two sandy ones OPA3-4 with high fracture intensities exhibited a limited permeability reduction to 10^{-15} – 10^{-14} m^2. During further consolidation at higher stresses, COX3 and OPA3 showed some fluctuations of the permeability. The dropping might reflect local collapse of fracture walls and clogging of the pathway, and on contrary, the rising might be caused by widening of some narrower pores due to possible erosion and movement of fine particles from the surfaces under the applied injection pressures (P_w = 0.1 – 1.0 MPa). As mentioned earlier, the deviatoric stress applied to OPA2-4 in group 2 sheared the matrix, disconnected the pathways locally, and hence decreased the permeability too. Moreover, by comparing the results from the different samples, one can identify some more effects as follows.

Effect of mineralogical composition

The samples in group 1 with similar initial fractures (figure 2.4a) and under same load conditions (figure 4.8a) showed large differences in water permeability. K_w–values of the clay-rich COX1 are one and four orders of magnitude lower than those of the sandy OPA1 and the carbonate-rich COX3, respectively. This is also true for the large samples with high fracture intensities in group 3 (figure 4.8c), i.e. K_w–values of the clay-rich COX2 being one order lower than those of the carbonate-rich COX4-6. As discussed above, the fracture sealing is determined mainly by the swelling capacity of the claystone, which is in turn determined by its mineralogical composition, particularly the fraction of clay minerals. The more clay content can take up more water, leading to more swelling and slaking of the fracture walls and clogging the interstices more effectively.

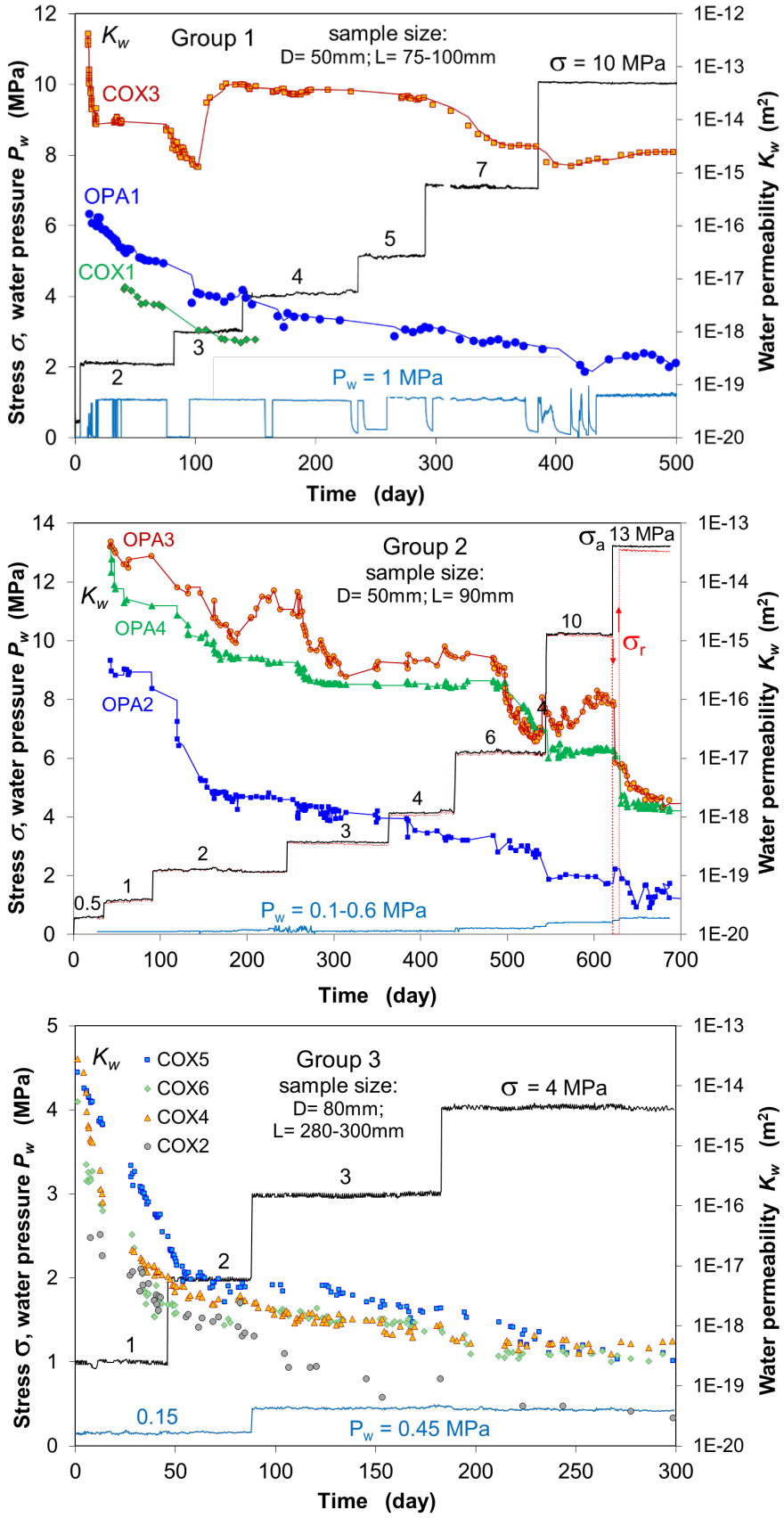

Fig. 4.8 Evolution of the water permeability measured on the fractured COX and OPA claystone samples during water injection under increased confining stresses

Effect of fracture intensity

The OPA sandy samples in groups 1 and 2 had been fractured to different geometries or intensities (figures 2.4a-b). The water permeabilities of samples OPA3 with three parallel fractures and OPA4 with a wide aperture of 2 mm (figure 4.8b) are two to three orders higher than those of the relatively less fractured ones OPA1 with a single fracture (figure 4.8a) and OPA2 with three but one inclined to a dead end (figure 4.8b). This demonstrates the significance of fracture intensity (density, aperture, connectivity, etc.) for the fracture permeability, particularly for the initial value. With water flow, the initial sharp fracture patterns tend to disappear to mud, in which the fracture voids are redistributed more homogeneously (figure 4.7b). Further variation of the permeability is dominated by the fraction of mud and its density. The larger the fracture aperture and density, the more fraction of mud, and thus the higher the porosity and permeability of the sample. Therefore, the initial permeability differences between the samples with different fracture intensities maintained relatively during the later consolidation. As mentioned earlier, the extremely high fracture density in OPA3 and the single wide aperture in OPA4 do not or rarely represent the realistic fractures in the EDZ.

Scale effect

A scale effect can be recognized by comparing the water permeabilities of the large samples COX 4-6 (D/L = 80/(280 – 300) mm; figure 4.8c) and the small one COX3 (D/L = 50/80 mm; figure 4.8a) from the same borehole in the carbonate-rich unit. The large samples, even though more intensively fractured (figure 2.4c), showed low K_w–values of ~$3x10^{-19}$ m^2 at a stress of 4 MPa, being four orders lower than that of the small sample even at higher stresses up to 10 MPa. As mentioned earlier, the distribution of carbonates is heterogeneous in form of bands on cm – dm scale (figure 2.1). If a fracture network is distributed through both carbonate-rich and clay-rich regions, the self-sealing performance of the entire network is determined mainly by the part of the network in the clay-rich region due to high sealing capacity, less dependent upon the other part in the carbonate-rich region with high stiffness. Therefore, it is important to take representative sample sizes for laboratory tests and large areas for field experiments for providing reliable data transferable for the realistic damaged rock mass.

4.2.1.3 Stress dependence of fracture sealing

The two key parameters of the fracture sealing, the fracture closure (or compaction) and water permeability, are strongly dependent on the applied stress. As a typical example, the radial and volumetric strains (ε_r and ε_v) and the water permeabilities K_w obtained on samples OPA2/4 at the end of each load step (figure 4.6) are depicted in figure 4.9 as a function of effective hydrostatic stress ($\sigma_{eff} = \sigma - ½ P_w$). As mentioned earlier, the radial strain reflects the closure of the fractures parallel to the sample axis. In case of the tests, there were also some micro-fractures randomly distributed and connected to the fracture network. Therefore, the volumetric strain is also needed for characterising the sealing of the fracture network. The measured data in figures 8a-b show that the fracture closure (ε_r, ε_v) increases non-linearly with increasing the effective stress and the associated water permeability decreases non-linearly too. In fact, the water permeability is directly related to the fracture closure, which can be approximately approached by

$$K_w = K_{wi}\, exp(-\alpha\, \varepsilon_r) \qquad (4.1)$$

where K_{wi} is the initial water permeability and α is a fitting parameter. The $K_w - \varepsilon_r$ data in figure 4.9c can be reasonably fitted by the empirical model with α = 8 and K_{wi} = 8x10^{-18} m^2 for OPA2 and α = 12 and K_{wi} = 2x10^{-14} m^2 for OPA4, respectively. The underestimation of the initial value for OPA2 is due to a lack of swelling/slaking effect at the beginning. A similar modelling result is also provided for the relation of water permeability to volumetric strain ($K_w - \varepsilon_v$) with different α - values of 3 for OPA2 and 4.5 for OPA4 (figure 4.9d). Because the fractures in the claystones lose the initial features with closing and clogging during water flow under confining stress, it is difficult or impossible to establish a constitutive model for the permeability in direct relation to the fracture feature for such a claystone as usually done for conventional geomaterials.

For comparison, these K_w–data are summarized in figure 4.10 as a function of the effective stress for most of the samples including the previous results from the clay-rich samples COX7-10 /ZHA 13/. The data from samples COX3 and OPA3-4 with unrepresentative sizes und fracture intensities are not involved. The dependence of water permeability on effective stress can be approximated by an exponential equation

$$K_w = K_{wo}\, exp\left(-\beta\, \sigma_{eff}\right) \qquad (4.2)$$

where K_{wo} is the initial water permeability at zero stress σ_{eff} = 0 and β is a parameter characterising the compressibility of the pathways.

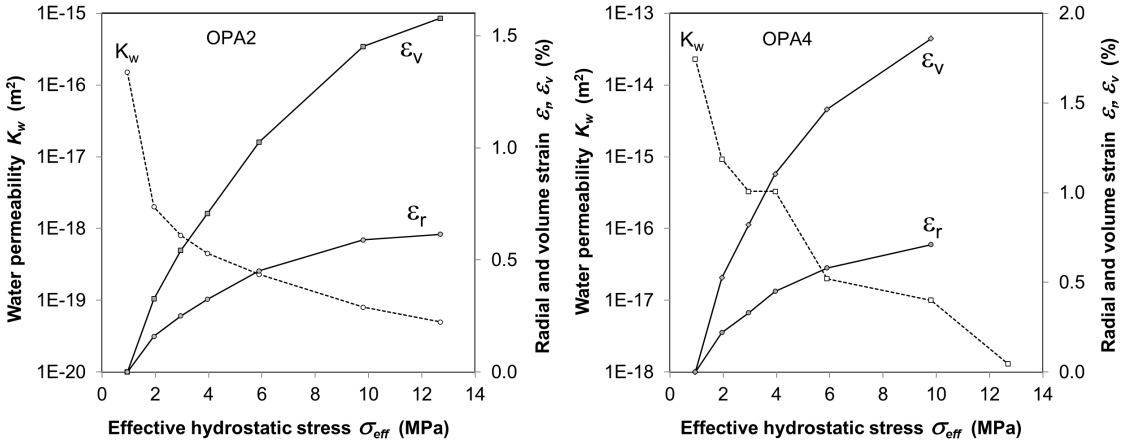

a. sample OPA2 with a high initial fracture density

b. sample OPA4 with a regular fracture aperture of 2 mm

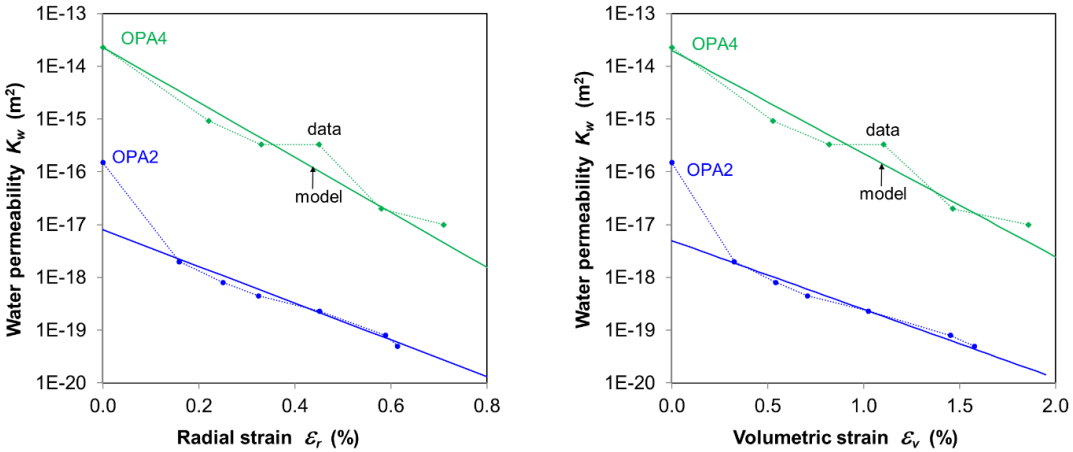

c. water permeability – radial compaction

d. water permeability – volumetric compaction

Fig. 4.9 Dependences of fracture closure (radial and volumetric compaction) and water permeability on effective hydrostatic stress; and fracture closure – water permeability relationship

As discussed above, the water-induced sealing of fractures and the associated permeability reduction is strongly dependent on the clay content. As shown in figure 4.10, the clay-rich samples COX1-2 and COX7-10 exhibited low initial permeabilities K_{wo} = 10^{-19} – 10^{-17} m^2, lower than K_{wo} = 10^{-17} – 10^{-16} m^2 of the carbonate-rich COX4-6 and the sandy OPA1-2. The high permeabilities are consistent with those of the EDZ near drift walls and the low values represent those in the deep EDZ region as observed at URLs Bure and Mont-Terri /ARM 14/ /DE 15/ /BOS 17/ HAL 21/. The slope of the $log(K_w)$–σ_{eff} curve varies mainly with mineralogical composition and fracture intensity, which is reflected by the parameter β ranging from 0.15 to 0.8 MPa^{-1} for the samples. A high β–value implies a high significance of the mechanical impact on the fracture sealing.

Generally, the test results from the representative samples showed significant self-sealing of fractures in the clay-, carbonate- and sand-rich claystones. Most of the fractured samples reached very low water permeabilities of 10^{-18} – 10^{-20} m^2 even at relative low stresses of 2 – 4 MPa. These values are close to that of the intact claystone, determined to 10^{-20} – 10^{-21} m^2 on the intact clay-rich COX samples under the *in-situ* rock conditions of a hydrostatic stress of 14 MPa and a pore pressure of 4.5 MPa (s. chapter 4.1). By extrapolation of the test data to the *in-situ* conditions, a complete recovery of the EDZ can be expected with a long-term consolidation phase of tens of thousands of years. This important conclusion needs to be confirmed further with more representative samples in size and fracture intensity like *in-situ*.

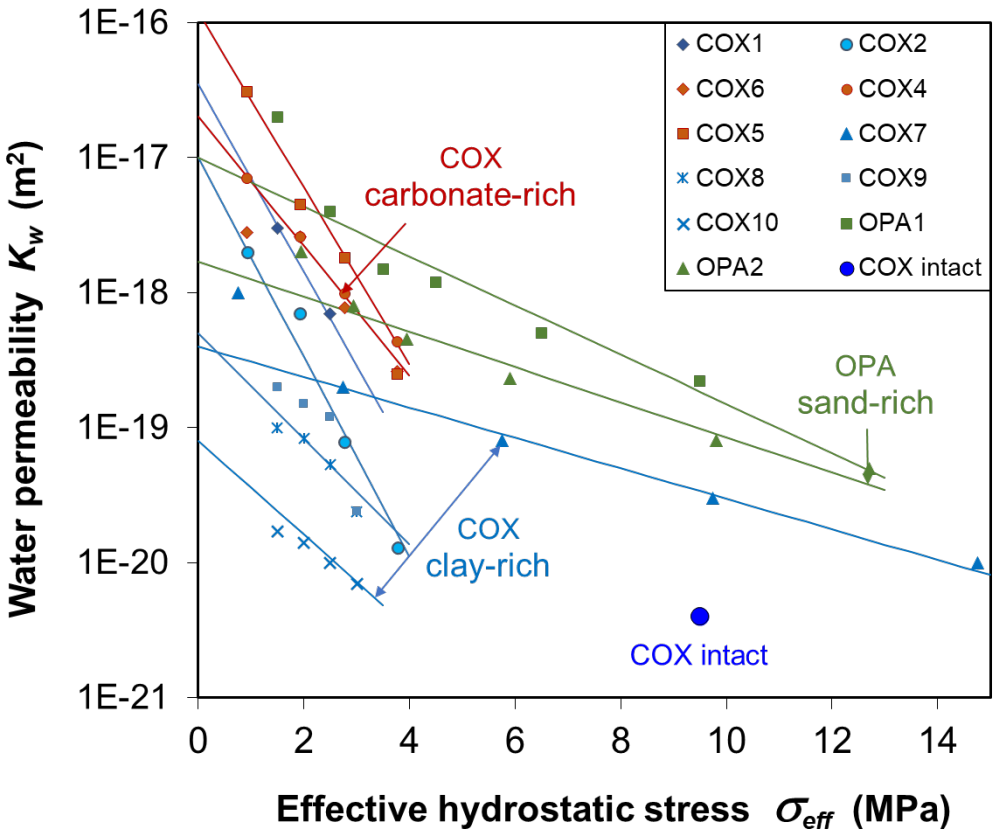

Fig. 4.10 Water permeabilities of the fractured claystone samples as a function of effective stress (blue colour for the clay-rich COX, red for the carbonate-rich COX, green for the sandy OPA)

4.2.2 Gas penetration and resealing of gas pathways

Gas testing followed the last consolidation stage at respective constant stress of 10, 13 and 4 MPa for the samples in group 1, 2 and 3 in order to investigate gas penetration

through sealed fractures and recovery of gas-induced pathways. The results obtained are illustrated in figures 4.11, 4.12 and 4.13, respectively.

4.2.2.1 Gas penetration

Gas injection pressure P_g was stepwise increased with small increments of 0.1 to 0.3 MPa at time intervals of 1 – 3 days. As gas bubbles were detected at the outlet side, the inlet pressure was defined as the gas breakthrough pressure P_b. In each group, the gas breakthrough event took place sequentially starting from a weakly sealed sample at a low pressure to the strongly sealed one at an increased pressure. For instance, the data in figure 4.11 show that the gas breakthrough event occurred firstly at a pressure P_b = 1.1 MPa at the weakly sealed COX3 with a water permeability of $K_w = 2x10^{-15}$ m^2 and then followed at P_b = 5.5 MPa at the strongly sealed OPA1 with a lower K_w – value of $2x10^{-19}$ m^2. Similar results were also obtained on the other samples, as shown in figures 4.12 and 4.13. This suggests that the strongly sealed fractures possess high capillary thresholds, which are to overcome by higher pressures for gas entering and percolating through the sealed fractures. After a network of gas pathways is generated at the breakthrough pressure, its gas permeability increases with further increasing gas pressure as shown in figures 4.12 and 4.13. That may be caused by newly generated fissures and dilatation of the pathways. As the gas injection was switched off after breakthrough (figure 4.11), the gas pressure fell and declined gradually with time to a lowest constant value. The minimum pressure is referred as the shut-in pressure P_{in}, at which the pathway network is disconnected.

4.2.2.2 Gas breakthrough pressure

The gas breakthrough pressures determined for the samples are summarized in table 4.2. As mentioned above, the gas breakthrough pressure depends on the sealing intensity of the fractures, which can be represented by the intrinsic or water permeability.

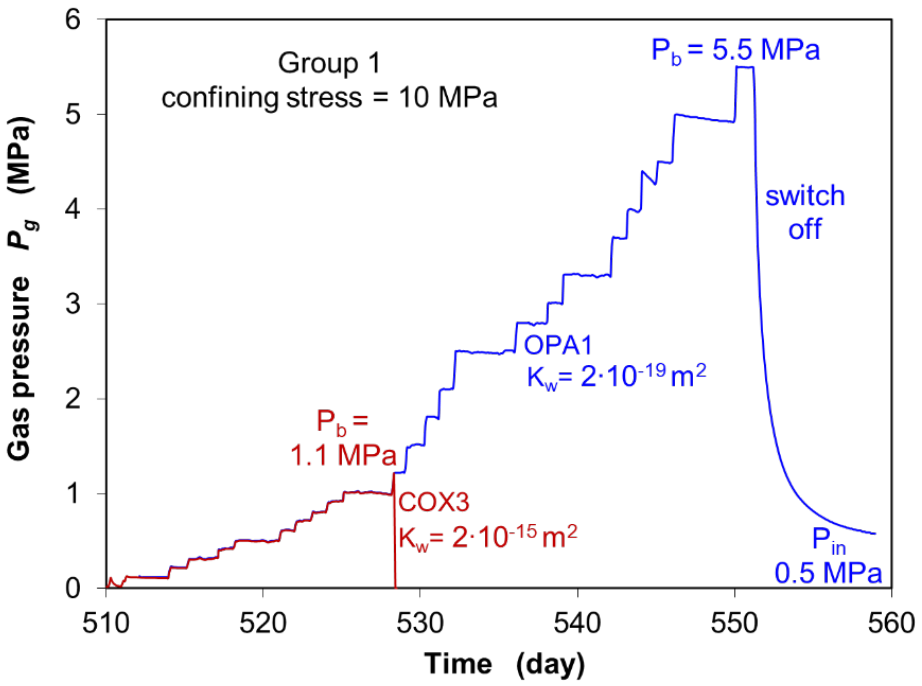

Fig. 4.11 Results of the gas penetration test (group 1) on water-saturated and fracture-sealed claystone samples at a hydrostatic stress of 10 MPa

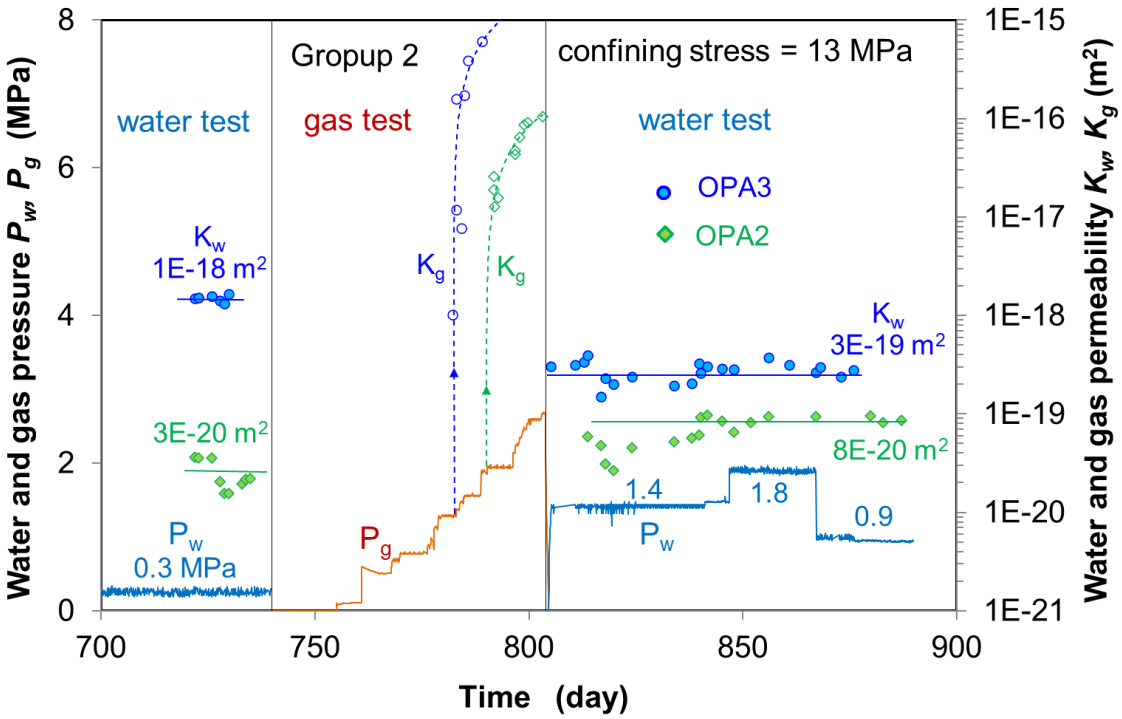

Fig. 4.12 Results of the gas penetration test (group 2) on water-saturated and fracture-sealed claystone samples and resealing of the gas-induced pathways by water flow at a hydrostatic stress of 13 MPa

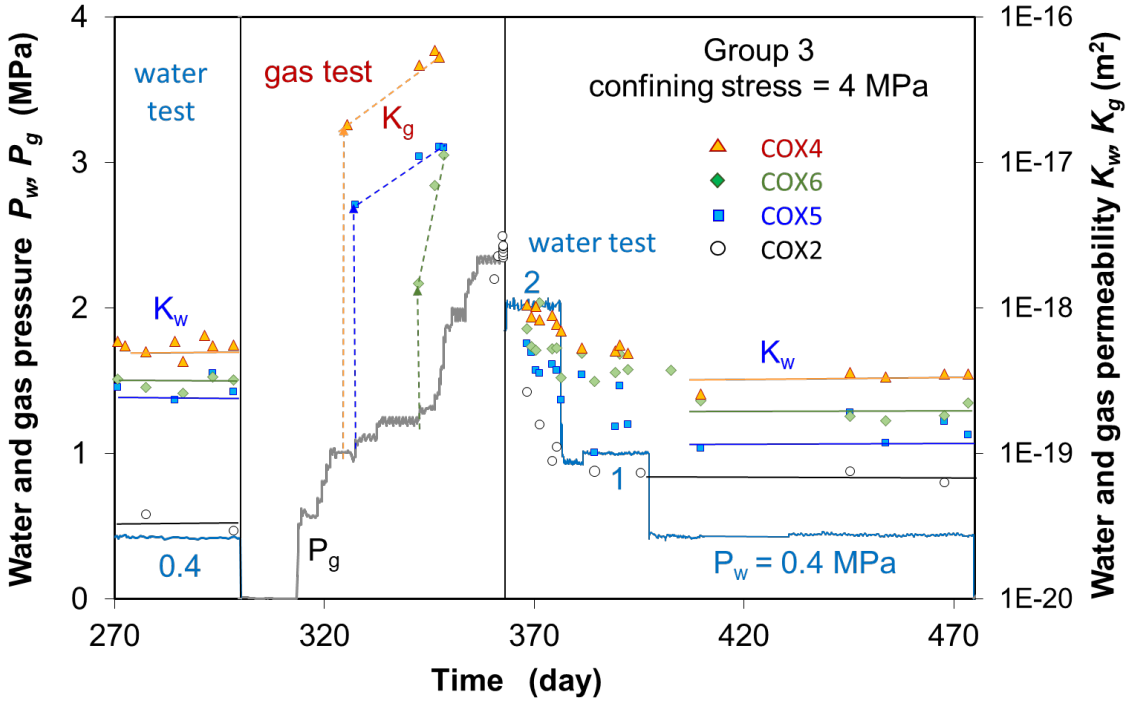

Fig. 4.13 Results of the gas penetration test (group 3) on water-saturated and fracture-sealed claystone samples and resealing of the gas-induced pathways by water flow at a hydrostatic stress of 4 MPa

Tab. 4.2 Results of measured *g*as breakthrough pressure P_b, water permeability K_{wa} before and K_{wb} after gas penetration through the water-saturated and fracture-sealed samples under various confining stresses σ

Group	Sample	σ (MPa)	P_b (MPa)	K_{wa} (m^2)	K_{wb} (m^2)
1	COX3	10	1.1	$2x10^{-15}$	-
	OPA1	10	5.5	$2x10^{-19}$	-
2	OPA2	13	2.0	$3x10^{-20}$	$8x10^{-20}$
	OPA3	13	1.3	$1x10^{-18}$	$3x10^{-19}$
3	COX2	4	2.3	$3x10^{-20}$	$6x10^{-20}$
	COX4	4	1.0	$6x10^{-19}$	$3x10^{-19}$
	COX5	4	1.1	$3x10^{-19}$	$1x10^{-19}$
	COX6	4	1.2	$3x10^{-19}$	$2x10^{-19}$

Extensive theoretical studies and experimental measurements in laboratory and in situ in different rocks such as plastic clay, hardened shale, limestone, anhydrite, and bedded salt /VOL 95/ /HOR 96/ /ROD 99/ suggest that the gas breakthrough pressure P_b is reciprocally dependent on the cube root of water permeability K_w

$$P_b = B\ (K_w)^{-1/n} \tag{4.3}$$

where B and n = 3 are parameters. This relationship is also confirmed by the previous experiments on the COX and OPA claystone samples with sealed fractures /ZHA 15/. An empirical model was also proposed there for a relationship of the gas breakthrough pressure to the minimum principal stress σ_{min}

$$P_b = B\ (K_{wo})^{-1/n}\ exp(\lambda\ \sigma_{min}) \tag{4.4}$$

By fitting the present data in table 4.2 and the previous ones in /ZHA 15/, average values of the parameters are obtained: B = 3.5×10^{-7} MPa·m$^{2/3}$, n = 3, λ = 0.2 MPa^{-1}, but different K_{wo} – values in a range of 8×10^{-20} to 1×10^{-17} m^2 representing the sealing intensities of the fractures in the samples. Figure 4.14 shows a reasonable agreement between the model curves and test data. Obviously, the gas breakthrough pressure increases with increasing the hydrostatic stress and with decreasing the water permeability. This model also fits the data obtained on the intact COX and OPA samples in our own and other tests /HAR 17/ /ROM 13/ and observed *in-situ* at URL Bure /DE 15/. The gas breakthrough pressures of the intact samples and rock mass are quite high up to 10 – 12 MPa, but still below the applied confining stresses and the gas fracturing boundary of the intact rock:

$$P_b < P_{fr} = \sigma_{min} + \sigma_T \tag{4.5}$$

where σ_T is the tensile strength of 1 – 2 MPa for the intact claystones /BOC 10/. Because the gas breakthrough pressures of the sealed claystone are always lower than the intact one, the EDZ, even when highly sealed, can still act as preferable pathways for gas release without compromising the integrity and barrier function of the host rock.

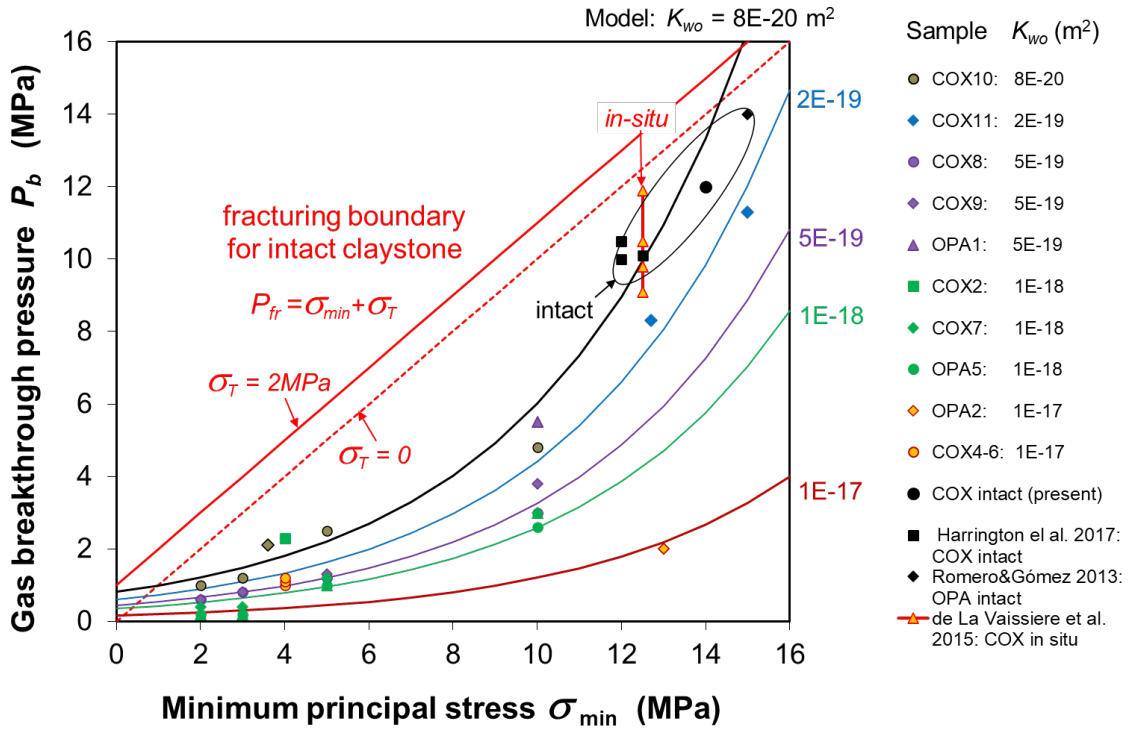

Fig. 4.14 Gas breakthrough pressures of the resealed and intact claystones as a function of minimum principal stress and initial water permeability

4.2.2.3 Resealing of gas pathways

Recovery of the gas-induced pathways was examined by measuring water permeability again and comparing with that before the gas penetration. The measurements were carried out at different injection pressures to examine effect of porewater pressure: P_w = 1.4, 1.8 and 0.9 MPa for the samples OPA2-3 (figure 4.12); and P_w = 2, 1 and 0.4 MPa for COX2/4-6 (figure 4.13). Though the selected injection pressures are limited below the *in-situ* porewater pressures (4.5 MPa in the COX formation at URL Bure), the corresponding hydraulic gradients are much higher than the *in-situ* ones and may affect the pathways. At a high stress of 13 MPa, samples OPA2-3 exhibited insignificant variation of K_w with P_w. In contrast, samples COX2/4-6 at a low stress of 4 MPa showed relatively high initial K_w – values at a high injection pressure P_w = 2 MPa, indicating a dilatancy of the pathways. However, the subsequent reduction of the injection pressure increased the effective stress, compressed the pathways, and thus decreased the permeability.

It is interesting to compare the water permeabilities measured before and after gas penetration. Most of the samples (OPA3, COX4-6) exhibited somewhat lower K_w – values

after the gas penetration than before, suggesting more consolidation of the pathways with time. In contrast, the strongly resealed samples OPA2 and COX2 with very low K_w–values of $6x10^{-20}$ – $3x10^{-20}$ m^2 showed a slight increase of K_w after gas penetration. This might be attributed to the effect of the previous dilatancy of the pathways caused by the high injection pressures. Further consolidation and permeability reduction of the pathways could be expected if the load continued for longer time periods. Generally, the very low water permeability values measured after gas penetration yield an important conclusion that the gas-induced pathways in the different kinds of claystones can reseal again against water flowing through.

4.2.2.4 Long-term gas migration

In order to understand long-term gas migration through the resealed pathways, the gas was injected simultaneously into the resealed gas pathways in the four large samples COX2 and COX4-6 for longer time periods. Figures 4.15 and 4.16 show the evolution of the inlet gas pressure and outflow rates of the samples as “a whole resealed EDZ” during the first and second injection phases of more than two months each, respectively. The confining stress was kept at 4 MPa.

During the first phase, the gas pressure P_{gi} was stepwise increased with a controlled gas inflow rate of 0.04 mL/min. At P_{gi} = 1.3 MPa, gas outflow was firstly detected on samples COX2 and COX 5-6 (point A in figure 4.15a). With gas escape, the pressure dropped down slightly. The pressure rising/dropping repeated sequentially to the next higher peaks of 1.5 and 1.8 MPa. From the maximum, the pressure dropped largely down to 0.9 MPa due to more quick release of gas. After a slight pressure increase again, a breakthrough occurred at the last sample COX4 (point D in figure 4.15b) with very quick gas release. This resulted in a further reduction of the gas pressure to a low level of 0.23 MPa over ~5 days. After shutting off the inlet, the gas pressure decreased to a low constant shut-in pressure of 0.14 MPa.

The second gas injection followed in the same way, yielding a maximum breakthrough pressure of 1.1 MPa, at which a rapid gas outflow was recorded at COX2. During the relaxation of the gas pressure, gas outflow was sequentially detected at COX6 at P_{gi} = 0.7 MPa, COX5 at P_{gi} = 0.4 MPa and COX4 at P_{gi} = 0.3 MPa. As the pressure reached at the minimum of 0.23 MPa, it increased slowly again to a constant at 0.25 MPa. The following shut-off led to a pressure decrease of 0.16 MPa.

The test data indicate that the advective movement of gas through the resealed samples varies temporally and spatially, reflecting unstable pathways with multiple opening/sealing processes. A question, if a steady gas flow will be reached over the much longer time periods under the repository conditions, needs to be answered in the future.

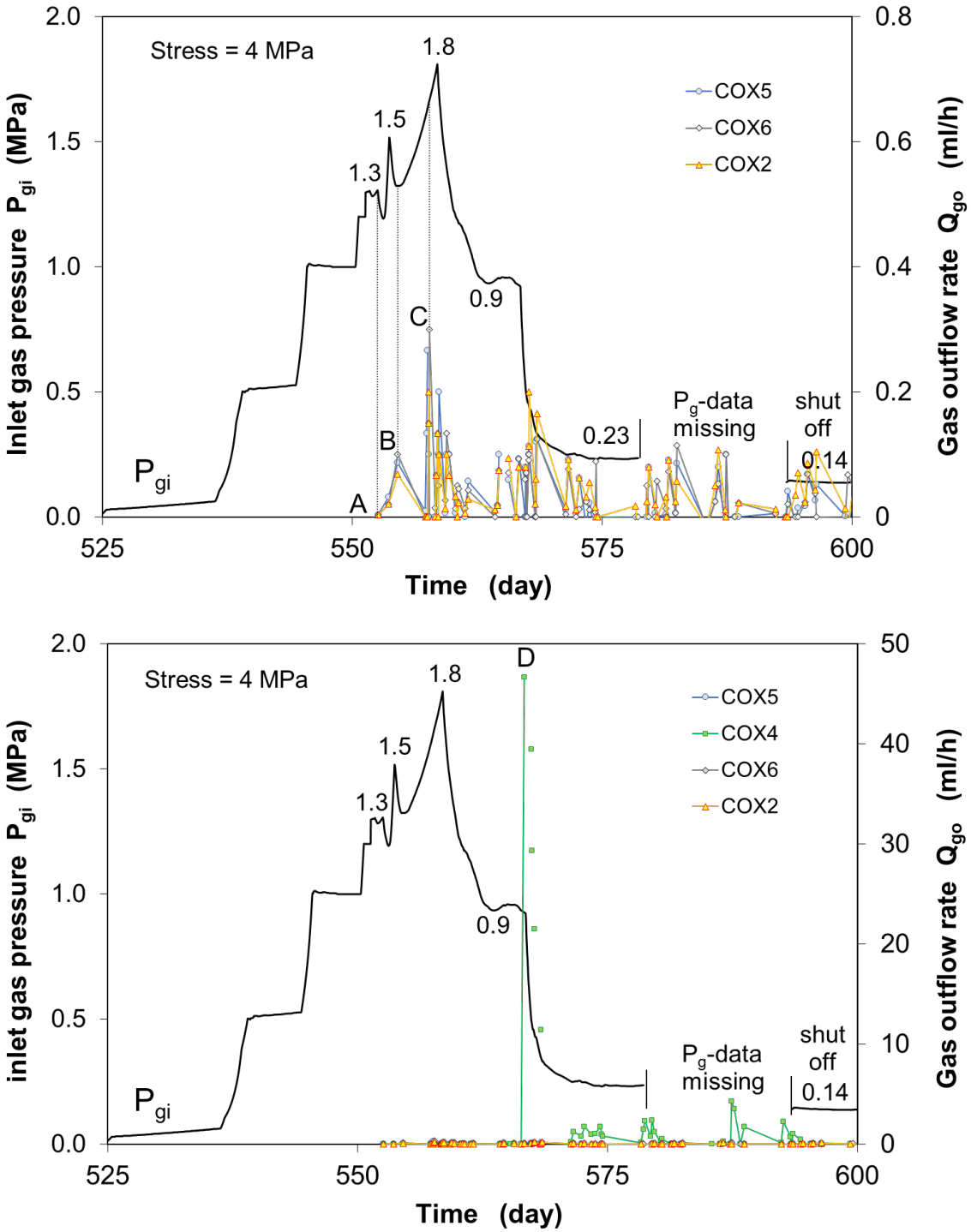

Fig. 4.15 Long-term evolution of the inlet gas pressure and outflow rates obtained on the fractured resealed COX samples during the first phase

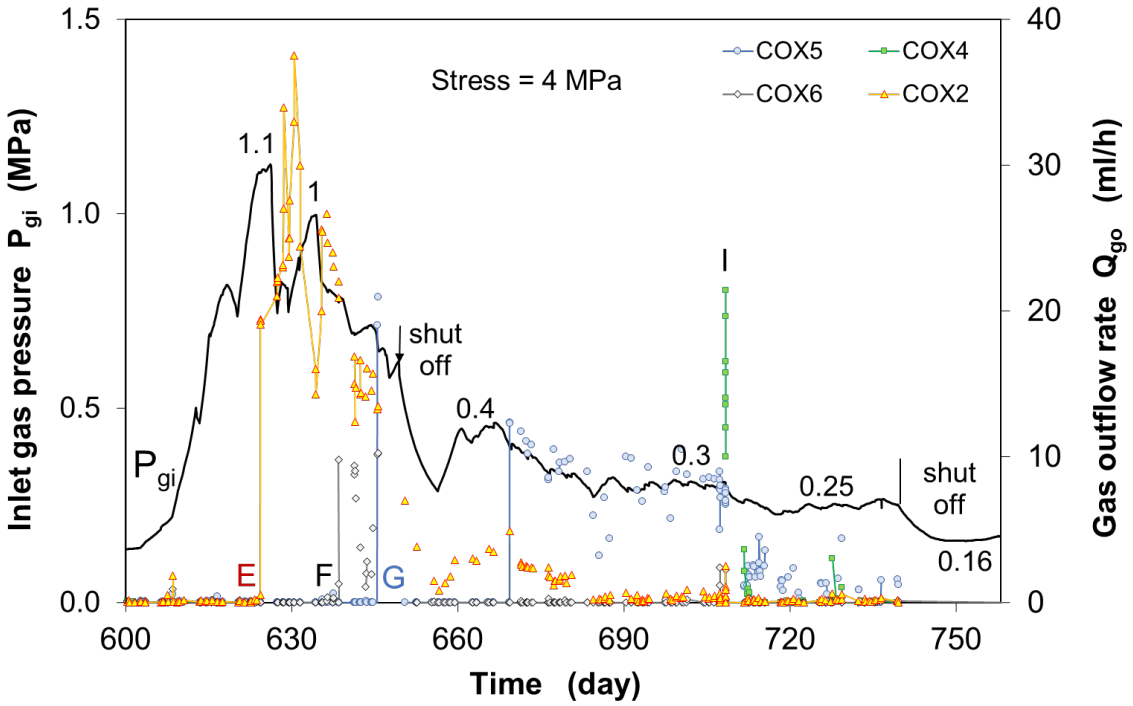

Fig. 4.16 Long-term evolution of the inlet gas pressure and outflow rates obtained on the fractured resealed COX samples during the second phase

5 Conclusions

The self-sealing performance of fractures in the clay- and carbonate-rich units of COX and the sandy facies of OPA clay formations was investigated on artificially fractured samples by measurements of fracture closure, water permeability, gas penetration, and recovery of gas-induced pathways. Most of the fractured samples with different sizes and fracture intensities represent the excavation damaged zone.

Under the combined impact of mechanical compression and water-induced clay swelling, the fractures in the different claystones tend to seal to very low water permeabilities close to the intact rock, depending on mineralogical composition, fracture intensity, confining stress, and time. The self-sealing capacity of the clay-rich claystone is higher than that of the carbonate-rich and sandy ones. A significant scale effect was identified, which indicates the importance of representative sample size and fracture intensity for providing reliable data transferable for the realistic damaged rock.

The sealed fractures become gas tight for certain pressures. The gas breakthrough pressure increases as the reciprocal of the cube root of water permeability and exponentially with increasing confining stress. However, the gas breakthrough pressures observed on the sealed and intact claystones are still lower than the applied confining stresses and lower than the gas-fracturing pressure of the intact rock. This implies that the EDZ can act as a preferable route for gas release without compromising the integrity of the host rock. Moreover, the gas pathways can reseal again to hinder water transport. The significant self-sealing capacities of the studied claystones guarantee the long-term insolation of radioactive waste. These important conclusions need to be confirmed further with more precise experiments in laboratory and in situ.

6 Acknowledgements

This work was co-funded by the European Commission (EC) from the European Union's Horizon 2020 research and innovation programme (EURAD) under grant agreement No 847593 and by the German Federal Ministry for the Environment, Nature Conservation, Nuclear Safety and Consumer Protection (BMUV) under contract number 02E11627.

We also gratefully acknowledge the support from the French Agence Nationale pour la Gestion des Déchets Radioactifs (Andra) and the National Cooperative for the Disposal of Radioactive Waste (Nagra) for providing the testing materials and fruitful discussions.

7 References

/AND 05/ Andra, DOSSIER 2005. Synthesis – Evaluation of the feasibility of a geological repository in an argillaceous formation. https://www.andra.fr/download/andra-international-en/document/266va.pdf

/ARM 14/ Armand, G., Leveau, F., Nussbaum, C., de La Vaissiere, R., Noiret, A., Jaeggi, D., Landrein, P., Righini C., 2014. Geometry and properties of the excavation-induced fractures at the Meuse/Haute-Marne URL drifts. Rock Mechanics and Rock Engineering 2014; 47(1): 21-41.

/AUR 15/ Auvray, C., Grgic, D., Morlot, C., Fourreau, E., Talandier, J., 2015. X-ray tomography applied to self-sealing experiments on argillites, Conference: ISRM 2015: The 13th International Congress of ISRM, "Innovations in Applied and Theoretical Rock Mechanics".

BOC 10/ Bock, H., Dehandschutter, B., Martin, C.D., Mazurek, M., de Haller, A., Skoczylas, F., Davy, C., 2010. Self-sealing of fractures in argillaceous formations in the context of geological disposal of radioactive waste – Review and synthesis. NEA Report No. 6184. OECD.

/BOS 04/ Bossart, P., Trick, T., Meier, P.M., Mayor, J.C., 2004. Structural and hydrogeological characterisation of the excavation-disturbed zone in the Opalinus Clay (Mont Terri Project, Switzerland), Applied Clay Science 2004; 26(1-4): 429-48.

/BOS 17/ Bossart, P., Jaeggi, D., Nussbaum, C., 2017. Experiments on thermo-hydro-mechanical behaviour of Opalinus Clay at Mont Terri rock laboratory, Switzerland, Journal of Rock Mechanics and Geotechnical Engineering 9 (2017), 502-510.

/CON 18/ Conil, N., Talandier, J., Djizanne, H., de La Vaissière, R., Righini-Waz, C., Auvray, C., Morlot, C., Armand, C., 2018. How rock samples can be representative of in-situ condition: a case study of Callovo-Oxfordian claystones, Journal of Rock Mechanics and Geotechnical Engineering10 (2018) 613-623.

/DE 15/ De La Vaissiere, R., Armand, G., Talandier, J., 2015. Gas and water flow in an excavation-induced fracture network around an underground drift: A case study for a radioactive waste repository in clay rock, Journal of Hydrology 521 (2015) 141–156.

/DON 19/ Donna, A.D., Charrier, P., Salager, S., Bésuelle, P., 2019. Self-sealing capacity of argillite samples, E3S Web of Conferences 92, 03005 (2019), 7th International Symposium on Deformation Characteristics of Geomaterials (IS-Glasgow 2019). https://doi.org/10.1051/e3sconf/20199203005

/GIO 18/ Giot, R., Auvray, A., Talandier, J., 2018. Self-sealing of claystone under X-ray nanotomography, in Multiple Roles of Clays in Radioactive Waste Confinement (edited by Norris S, Neeft EAC & Van Geet M), Geological Society, London, Special Publications, 482. https://doi.org/10.1144/SP482.4.

/HAL 21/ Hale, S., Ries, X., Jaeggi, D., Blum, P., 2021. Mechanical and hydraulic properties of the excavation damaged zone (EDZ) in the Opalinus Clay of the Mont Terri rock laboratory, Switzerland. Solid Earth, 12, 1581–1600, 2021. https://doi.org/10.5194/se-12-1581-2021

/HAR 17/ Harrington, J.F., Cuss, R.J, Talandier, J., 2017. Gas transport properties through intact and fractured Callovo-Oxfordian mudstones. Geological Society, London, Special Publications 454 (1), 131–154.

/HOR 96/ Horseman, S.T., Higgo, J.W., Alexander, J., Harrington, J.F., 1996. Water, Gas and Solute Movement through Argillaceous Media. Report CC-96/1.

HOU 14/ Houben, M.E., Desbois, G., Urai, J., 2014. A comparative study of representative 2D microstructures in Shaly and Sandy facies of Opalinus Clay (Mont Terri, Switzerland) inferred form BIB-SEM and MIP methods, Marine and Petroleum Geology 49 (2014) 143-161.

/KAU 13/ Kaufhold, A., Gräsle, W., Plischke, I., Dohrmann, R., Siegesmund, S., 2013. Influence of carbonate content and micro fabrics on the failure strength of the sandy facies of the Opalinus Clay from Mont-Terri (Underground Rock Laboratory), Engineering Geology 156, 111-118. http://www.sciencedirect.com/science/article/pii/S0013795213000434.

/ISR 81/ ISRM (1981): Rock Characterization Testing & Monitoring – IRSM suggested methods, Commission on Testing Methods, International Society for Rock Mechanics.

/JOB 17/ Jobmann M, Bebiolka A, Burlaka V, Herold P, Jahn S, Lommerzheim A, Maßmann J, Meleshyn A, Mrugalla S, Reinhold K, Rübel A, Stark L, Ziefle G (2017): Safety assessment methodology for a German high-level waste repository in clay formations, Journal of Rock Mechanics and Geotechnical Engineering 9 (2017) 856-876.

/MAR 17/ Marschall, P., Giger, S., de La Vassiere, R., Shao, H., Leung, H., Nussbaum, C., Trick, T., Lanyon, B., Senger, R., Lisjak, A., Alcolea, A., 2017. Hydro-mechanical evolution of the EDZ as transport path for radionuclides and gas: insights from the Mont Terri rock laboratory (Switzerland), Swiss J Geosci (2017) 110:173–194.

/MAZ 08/ Mazurek, M., Gautschi, A., Marschall, P., Vigneron, G., Lebon, P., Delay, J., 2008. Transferability of geoscientific information from various sources (study sites, underground rock laboratories, natural analogues) to support safety cases for radioactive waste repositories in argillaceous formations. Physics and Chemistry of the Earth, Vol. 33, 95-105.

/NAG 02/ Nagra, 2002. Project Opalinus Clay. Safety Report. Demonstration of disposal feasibility for spent fuel, vitrified high-level waste and long-lived intermediate-level waste. Nagra Tech. Rep. NTB 02-05. Nagra, Wettingen (2002b).

/PEA 03/ Pearson, F.J., Arcos, D., Bath, A., Boisson, J.Y., Fernandez, A.M., Gäbler, H.E., Gaucher, E., Grifault, L., Hernan, P., Waber, H.N., 2003. Mont Terri Project – Geochemistry of Water in the Opalinus Clay formation at the Mont Terri Rock Laboratory, Reports of the FOWG, no. 5, 2003, Bern.

/ROD 99/ Rodwell, W.R., Harris, A.W., Horseman, S.T., Lalieux, P., Müller, W., Ortiz, A.L., Pruess, K., 1999. Gas Migration and Two-Phase Flow through Engineered and Geological Barriers for a Deep Repository for Radioactive Waste. A Joint EC/NEA Status Report, European Commission, EUR 19122 EN.

/ROB 15/ Robinet, J.C., Sardini, P., Siitara-Kauppi, M., Pret, D., Yven, B., 2015. Upscaling the porosity of the Callovo-Oxfordian mudstone from the pore scale to the formation scale; insights from the 3H-PMMA autoradiography technique and SEM BSE imaging. Sedimentary Geology, 321, 1–10.

/ROM 13/ Romero, E. and Gómez, R., 2013. Water and air permeability tests on deep core samples from Schlattingen SLA-1 borehole. Nagra Arb. Ber. NAB 13-51. Nagra, Wettingen, Switzerland.

/THU 99/ Thury, M. and Bossart, P., 1999. Mont Terri Rock Laboratory, Results of the hydrogeological, geochemical and geotechnical experiments performed in 1996 and 1997. Landeshydrologie und –geologie, Geologischer Bericht No. 23. Federal Officie of Topography (swisstopo), Wabern, Switzerland.

/VOL 95/ Volckaert, G., Ortiz, L., de Canniere, P., Put, M., Horseman, S.T., Harrington, J.F., Fioravante, V., Impey, M.D., 1995. MEGAS – Modelling and Experiments on Gas Migration in Repository Rocks, Final Report Phase 1, European Commission Report EUR 16235 EN, 1995.

/ZHA 10/ Zhang, C.L., Wieczorek, K., Xie, M.L., 2010. Swelling experiments on mudstones, Journal of Rock Mechanics & Geotechnical Engineering, 2010, 2(1), 41-47.

/ZHA 11/ Zhang, C.L., 2011. Experimental evidence for self-sealing of fractures in claystone, Physics and Chemistry of the Earth, Vol. 36, 2011, 1972-1980.

/ZHA 13/ Zhang, C.L., 2013. Sealing of Fractures in Claystone, Journal of Rock Mechanics and Geotechnical Engineering 5 (2013), 214-220.

/ZHA 15/ Zhang, C.L., 2015. Investigation of gas migration in damaged and resealed claystone, Geological Society Special Publication 415 – Gas Generation and Migration in Deep Geological Radioactive Waste Repositories (edited by SHAW, R.P.), The Geological Society of London, 75-93.

/ZHA 17/ Zhang, C.L., 2017. Response of clay rock to moisture change, in: Advances in Laboratory Testing and Modelling of Soils and Shales (ATMSS), Springer Series in Geomechanics and Geoengineering. DOI 10.1007/978-3-319-52773-4 17.

/ZHA 19/ Zhang, C.L., Komischke, M., Kröhn, M., Rogalski, A., Zehle, B., 2019. Experimental Study of the Mechanical Behaviour of the Sandy Facies of Opalinus Clay at Mont Terri, LT-A Programme within the Mont-Terri-Project, Gesellschaft für Anlagen- und Reaktorsicherheit (GRS), Braunschweig, GRS-555.

/ZHA 22/ Zhang, C.L. and Talandier, J., 2022. Self-sealing of fractures in indurated claystones measured by water and gas flow, J. Rock Mech. Geotech. Eng. https://doi.org/10.1016/j.jrmge.2022.01.014.

List of tables

List of figures

Gesellschaft für Anlagen- und Reaktorsicherheit (GRS) gGmbH

Schwertnergasse 1
50667 Köln
Telefon +49 221 2068-0
Telefax +49 221 2068-888

Boltzmannstraße 14
85748 Garching b. München
Telefon +49 89 32004-0
Telefax +49 89 32004-300

Kurfürstendamm 200
10719 Berlin
Telefon +49 30 88589-0
Telefax +49 30 88589-111

Theodor-Heuss-Straße 4
38122 Braunschweig
Telefon +49 531 8012-0
Telefax +49 531 8012-200

www.grs.de

ISBN 978-3-949088-95-7